ELSEVIER

Remote Sensing of Environment 76 (2000) 213–238

Remote Sensing of Environment

www.elsevier.com/locate/rse

Narrowband to broadband conversions of land surface albedo I Algorithms

Shunlin Liang*

Laboratory for Global Remote Sensing Studies, Department of Geography, University of Maryland, College Park, MD 20742, USA

Received 28 March 2000; accepted 10 November 2000

Abstract

Land surface broadband albedo is a critical variable for many scientific applications. High-resolution narrowband satellite observations contain important information that enables us to map land surface albedo globally, and validate the coarse-resolution albedo products from the broadband sensors using ground "point/plot" measurements. However, the conversions from narrowband to broadband albedos of a general surface type have not been well established. Most studies compute total shortwave albedo based on either the empirical relations between surface total shortwave albedo measurements and satellite observations or radiative transfer simulations with the limited number of surface reflectance spectra because of the computational constraints. As a result, many conversion formulae for the same sensors are quite different. In this study, we applied an approach that decouples surface reflectance spectra from the real-time radiative transfer simulations so that many different surface reflectance spectra and the atmospheric conditions can be effectively incorporated. The conversion formulae, based on extensive radiative transfer simulations, are provided in this paper for calculating the total shortwave albedo, total-, direct-, and diffuse-visible, and near-infrared broadband albedos for several narrowband sensors, including ASTER, AVHRR, ETM+/TM, GOES, MODIS, MISR, POLDER, and VEGETATION. Some of these formulae were compared with the published formulae of the same sensors and further validations using extensive ground measurements will be discussed in the companion paper.

1. Introduction

Land surface broadband albedo is a critical variable affecting the earth's climate (Cess, 1978; Dickinson, 1983; Kiehl et al., 1996). In semiarid regions, an increase in albedo leads to a loss of radiative energy absorbed at the surface, and convective overturning is reduced. As a result, precipitation decreases. Evaporation may also decrease, further inhibiting precipitation. Similar reductions in precipitation and evapotranspiration have been found for increased albedo in tropical Africa and the Amazon basin (Dirmeyer & Shukla, 1994). It has been well recognized that surface albedo is among the main radiative uncertainties in current climate modeling. Most global circulation models are still using prescribed fields of surface albedo, which are often 5–15% in error (relative error) from place to place and time to time (Dorman & Sellers, 1989; Sato et al., 1989). The recent data from the Boreal Ecosystem–Atmosphere Study (BOREAS) project found that the winter albedos of the forest sites were significantly different from those used in the European numerical weather prediction model, which led to a systematic underestimation of the near-surface air temperature (Sellers et al., 1997).

Remote sensing is the only practical means for mapping land surface albedo globally. Broadband albedo is usually estimated from broadband sensors. Measurements obtained with the Nimbus-7 Earth Radiation Budget (ERB) instrument (Jacobowitz et al., 1984), data from the Earth Radiation Budget Experiment (ERBE) (Smith et al., 1986) and the Scanner for the Earth Radiation Budget (ScaRaB) (Kandel et al., 1998) have yielded unique data sets that are a valuable source of knowledge of land surface broadband albedo. However, the accurate determination of land surface broadband albedo from top-of-atmosphere (TOA) observations requires the knowledge of the atmospheric conditions and surface characteristics, which can be monitored effectively only by multispectral sensors. Narrowband multispectral observations also have much finer spatial resolutions that allow us to characterize

* Tel.: +1-301-405-4556; fax: +1-301-314-9299.
E-mail address: sliang@geog.und.edu (S. Liang).

0034-4257/00/$ – see front matter
PII: S0034-4257(00)00205-4

both the surface and atmospheric heterogeneity. The derivation of surface broadband albedos from narrowband observations requires several levels of processing. Important steps include atmospheric correction, angular models that convert directional reflectance to spectral albedo, and narrowband to broadband conversion (e.g., Kimes & Holben, 1992; Ranson, Irons, & Daughtry, 1991). Some of these issues have been recently reviewed by Liang, Stroeve, Grant, Strahler, and Duvel (2000) and Lucht and Roujean (2000). We will primarily address the narrowband to broadband conversions in this study given land surface spectral albedos.

Surface broadband albedos are not the sole measures of surface reflective properties since they also depend on the atmospheric conditions. The downward flux distribution at the bottom of the atmosphere is the weighting function for converting spectral albedos to broadband albedos, and different atmospheric conditions have different downward flux distributions. Thus, surface broadband albedos retrieved under one specific atmospheric condition from remotely sensed data may not be applicable to other atmospheric conditions.

In our previous study (Liang, Strahler, & Walthall, 1999), we made a suggestion to separate inherent albedo and apparent albedo. Inherent albedo is totally independent of the atmospheric condition, and the apparent albedos are equivalent to those measured by albedometers or pyranometers in the field. If inherent albedos are provided, advanced users may transform them to apparent albedos at any atmospheric conditions that they need (Lucht, Schaaf, & Strahler, 2000). Particularly, when the atmospheric downward fluxes are known, integration with inherent albedo will produce much more accurate broadband albedo products. However, most users may not want to implement such a procedure for many practical applications in which high accuracy is not the top priority. Given narrowband albedos, the average broadband albedos need to be predicted under general atmospheric conditions. This is what most previous studies have done (e.g., Brest & Goward, 1987; Li & Leighton, 1992; Saunders, 1990; Stroeve, Nolin, & Steffen, 1997; Wydick, Davis, & Gruber, 1987). The formulae of Brest and Goward (1987), Li and Leighton (1992), and Wydick et al. (1987) are for converting TOA narrowband albedos to surface broadband albedos.

For two AVHRR reflective bands, Gutman (1994) and Saunders (1990) simply use 0.5 as their converting coefficients for calculating TOA shortwave albedo. Valiente, Nunez, Lopez-Baeza, and Moreno (1995) derive a conversion formula for calculating surface shortwave broadband albedo based on the 5S code and 20 surface reflectance spectra. Russell, Nunez, Chladil, Valiente, and Lopez-Baeza (1997) have come out with a different formula for converting nadir-view surface reflectance based on a set of ground observations. Stroeve et al. (1997) derive the surface broadband albedo over the Greenland ice sheet. Han, Stamnes, and Lubin (1999) calculate surface broadband albedo using a different formula suggested by Key (1996). When we group them as in Eq. (1):

$$\alpha_{\text{short}} = \begin{cases} 0.0442 + 0.441\alpha_1 + 0.67\alpha_2 & \text{Russell et al. (1997)} \\ 0.035 + 0.545\alpha_1 + 0.32\alpha_2 & \text{Valiente et al. (1995)} \\ 0.0034 + 0.34\alpha_1 + 0.57\alpha_2 & \text{Key (1996)} \\ 0.0412 + 0.655\alpha_1 + 0.216\alpha_2 & \text{Stroeve et al. (1997)}, \end{cases} \quad (1)$$

where α_1 and α_2 are AVHRR spectral albedos, it is obvious that they are quite different for the same AVHRR sensor. This demonstrates a need for a further study on this subject.

All these studies were based on either field measurements of certain surface types or model simulations. It is impossible to develop a universal formula only based on ground measurements because it is so expensive to collect extensive data sets over different atmospheric and surface conditions. Model simulation is a better approach to develop universal conversion formulae, and ground measurements are certainly valuable for validation.

In the previous studies, only a few dozens of surface reflectance spectra are usually used in the model simulations (e.g., Li & Leighton, 1992; Liang et al., 1999; Valiente et al., 1995) because of the computational constraints. In this study, we apply a method that allows us to incorporate as many representative surface reflectance spectra as we want without experiencing the formidable computational burden.

Most studies mentioned above provide conversion formulae for calculating only the total shortwave broadband albedo. In land surface modeling, the visible and near-infrared (IR) broadband albedos are quite often needed. Moreover, both total visible and near-IR broadband albedos are further divided into direct and diffuse albedos. For example, in the NASA Goddard Earth Observation System-Data Assimilation System (GEOS-DAS) assimilation surface model (Koster & Suarez, 1992), National Center for Atmospheric Research (NCAR) community climate model (Kiehl et al., 1996), and the simple biospheric model (Sellers et al., 1996; Xue, Sellers, Kinter, & Shukla, 1991), broadband visible and near-IR albedos are further divided into direct and diffuse albedos in both visible and near-IR regions. To calibrate and validate these land surface models, it is greatly desirable to generate direct and diffuse visible and near-IR broadband albedos directly from satellite observations.

The objective of this paper is to provide simple formulae for calculating average land surface broadband albedos (total shortwave albedo, total-, direct-, and diffuse-visible, and near-IR albedos) from a variety of narrowband sensors under various atmospheric and surface conditions.

2. Methods

The basic procedure is similar to that in our previous study (Liang et al., 1999), which was based on extensive MODTRAN simulations. Instead of MODTRAN, we employed the Santa Barbara DISORT Atmospheric Radiative Transfer (SBDART) code (Ricchiazzi, Yang, Gautier, & Sowle, 1998) in this study. SBDART has a nice interface that allows us to set-up simulations very effectively. Another major difference is that we ran SBDART without using real surface reflectance spectra. Specifically, SBDART was run three times with three surface reflectances (0.0, 0.5, and 0.8) for each atmospheric condition and solar geometry. Assume the surface is a Lambertian, the downward flux can be expressed by (Liou, 1980)

$$F = F_0 + \frac{r_s}{1 - r_s \overline{r}} \pi \mu_i E_0 \gamma(\mu_i) \overline{r} \tag{2}$$

where μ_i is the cosine of solar zenith angle (θ_i, SZA), F_0 is downward flux without surface contribution (i.e., surface reflectance is zero, $r_s = 0$), r is the spheric albedo of the atmosphere, E_0 is the TOA downward flux, and $\gamma(\mu_i)$ is the total atmospheric transmittance. Results from three runs of the SBDART form three equations that enable us to determine three unknowns (F_0, r, and $E_0\gamma(\mu_i)$) in the above equation. As long as these unknowns are determined, it is straightforward to calculate downward flux with any surface reflectance spectra by using Eq. (2).

Different surface reflectance spectra from the USGS digital spectral library (Clark, Swayze, Gallagher, King, & Calvin, 1993), from measurements by Dr. Salisbury at the Johns Hopkins University, and from the JPL spectral library were collected. Most of these spectra were measured in the laboratory. To account for the natural environment conditions, over one hundred of reflectance spectra of different surface cover types were extracted from AVIRIS (airborne visible–infrared imaging spectrometer) imagery, an airborne hyperspectral sensor (Green, Eastwood, & Williams, 1998). Depending on the spatial variations of surface reflectance, different window sizes were selected, and a median value was then calculated for each waveband. AVIRIS has 224 bands; unfortunately, we found 20 bands of little values because of noise or the absence of signals. Spectral reflectances (0.25–2.5 μm) were interpolated from the remaining 204 bands. In total, we employed 256 surface reflectance spectra in this study, including soil (43), vegetation canopy (115), water (13), wetland and beach sand (4), snow and frost (27), urban (26), road (15), rock (4), and other cover types (9). They have different wavelength dependences and magnitudes, from coastal water (low albedos) to snow and frost (high visible albedos). Eleven atmospheric visibility values (2, 5, 10, 15, 20, 25, 30, 50, 70, 100, and 150 km) were used for different aerosol loadings, and five atmospheric profiles (tropical, midlatitude winter, subarctic summer, subarctic winter, and US62) that also represent different water vapor and other gaseous amounts and profiles were utilized. A range of nine SZAs was simulated from 0° to 80° with the increment of 10°. SBDART was run at 231 spectral ranges with the increased wavelength increment from 0.0025 μm at the shortest wavelength end to 0.025 μm at the longest wavelength end.

After determining downward fluxes (direct and diffuse), the sensor spectral response functions were integrated with downward flux and surface reflectance spectra to generate narrowband spectral albedos. Broadband albedo is simply defined as the ratio of the upwelling flux (F_u) to the downward flux (F_d)

$$\alpha(\theta_i; \Lambda) = \frac{F_u(\theta_i; \Lambda)}{F_d(\theta_i; \Lambda)} = \frac{\int_{\lambda_1}^{\lambda_2} F_u(\theta_i; \lambda) d\lambda}{\int_{\lambda_1}^{\lambda_2} F_d(\theta_i; \lambda) d\lambda}, \tag{3}$$

where Λ is denoted to be the waveband from wavelength λ_1 to wavelength λ_2. In this study, three broad wavebands are specified, visible (0.4–0.7 μm), near-IR (0.7–2.5 μm), and total shortwave (0.25–2.5 μm). There exist different spectral ranges specified in the literature for the total shortwave broadband. The reason that we adopt this conservative range is because the measured surface reflectance values are usually available in this range and also downward fluxes beyond this range are very small under different atmospheric conditions so that their contributions to the total shortwave albedo are negligible. Diffuse and direct albedos are calculated by using only diffuse or direct fluxes in Eq. (3). Regression analyses were then conducted to generate different conversion formulae.

3. Broadband albedo characteristics

Spectral albedo has been well understood, but broadband albedos have not been widely discussed in the literature. Before providing different conversion formulae,

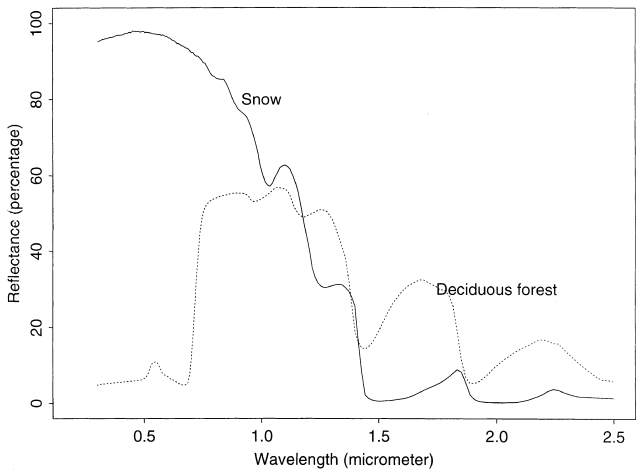

Fig. 1. Typical reflectance spectra of snow and deciduous forest.

it is helpful to examine the simulated surface broadband albedos. It is also a technique to make sure that the simulated data are reasonable.

Broadband albedo is not the sole measure of surface properties. It depends on the atmospheric conditions through downward fluxes that are the weighting function of the conversion from narrowband to broadband albedos. To illustrate this point quantitatively, let us examine two surface types (deciduous forest and snow) whose spectra are presented in Fig. 1. Fig. 2 shows the dependence of spectral downward fluxes on SZA and atmospheric visibility (low visibility representing very turbid atmosphere and high visibility very clear atmosphere). It is obvious that direct flux increases and diffuse flux decreases when the atmosphere varies from turbid (low visibility) to clear (high visibility). Total spectral downward fluxes decrease under both the clear and turbid atmospheric conditions.

Fig. 3 demonstrates how broadband albedos vary as the function of SZA and atmospheric visibility where the reflectance spectra of snow and deciduous forest are fixed. It is interesting to see that the total shortwave albedo of deciduous forest increase as SZA becomes larger, but the total shortwave albedo of snow has the opposite trend. It is because canopy has much larger reflectance in the near-IR spectrum, but snow has much

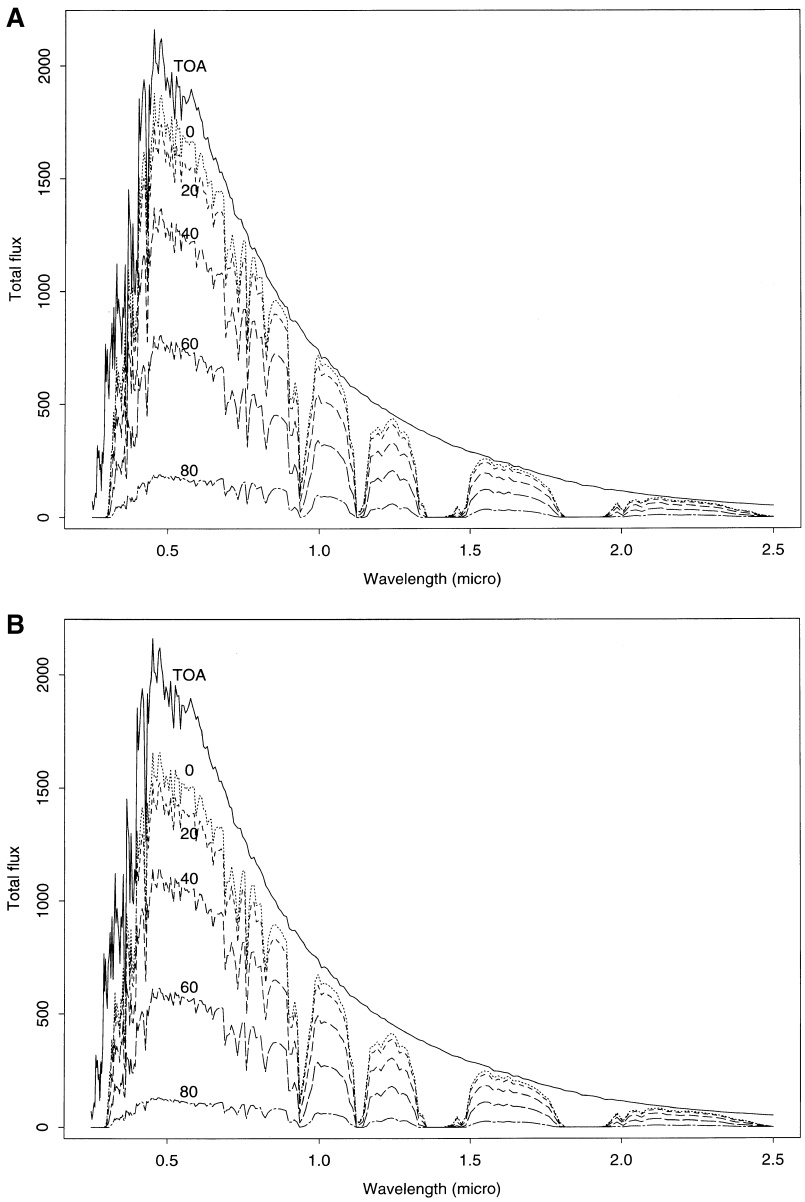

Fig. 2. Dependence of spectral downward fluxes (w/m^2/μm) on SZA (A: 30 km visibility; B: 5 km visibility) and atmospheric visibility at the solar zenith (C: direct flux; D: diffuse flux). 1976 US standard atmosphere.

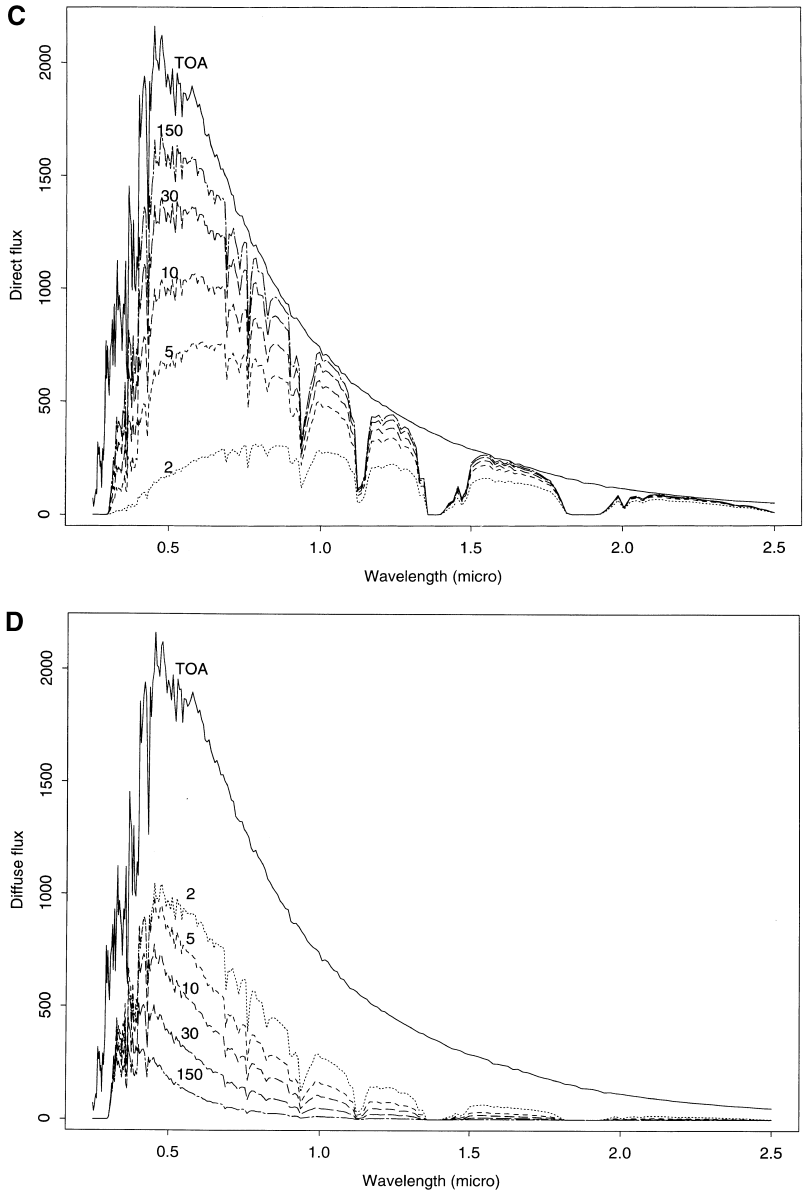

Fig. 2 (*continued*).

larger reflectance in the visible spectrum. When SZA becomes larger, the downward flux in the visible spectrum is reduced much faster than in the near-IR spectrum given a specific atmospheric condition, which indicates that the relative weights are smaller in the visible region and larger in the near-IR region. Total near-IR albedos for both snow and canopy do not change much as SZA and atmospheric visibility vary. If the total near-IR albedo is divided into direct and diffuse components, their dependences on SZA and the atmospheric visibility become much stronger. It is interesting to observe the asymptotic properties of total and diffuse near-IR broadband albedos. When the SZA is very large or the atmospheric visibility value is very low, both total and diffuse near-IR albedos are numerically very close because downward fluxes actually represent total downward flux under these conditions. For both snow and canopy, the total visible albedos (as well as the direct and diffuse components) are almost unchanged as we change the SZA and atmospheric visibility. Note that in this experiment, we assume both canopy and snow have constant reflectance spectra for different SZAs and atmospheric conditions. In fact, the spectral albedos of both snow and canopy depend on SZA. Thus, canopy and snow visible broadband albedos should change at different SZAs.

There are also several important features of broadband albedos that can be observed in Fig. 3. Unless the SZA

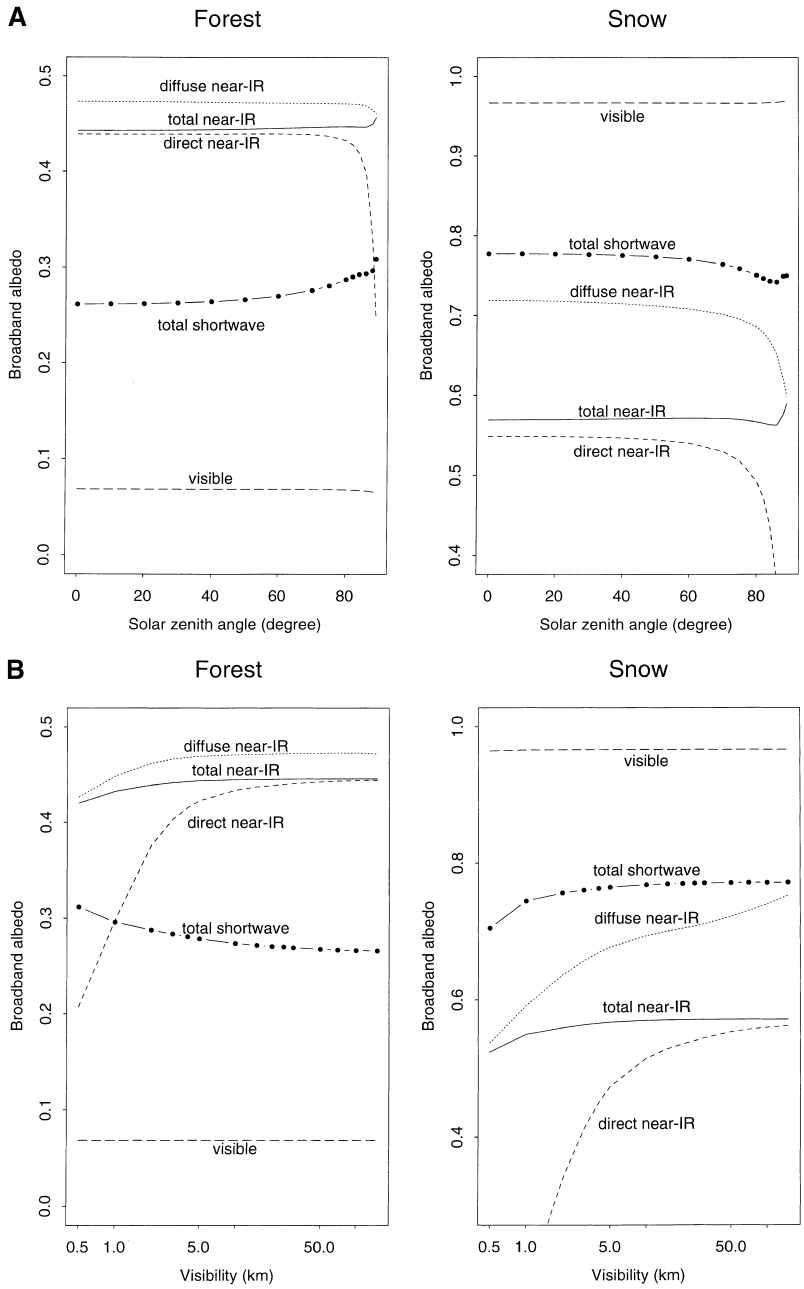

Fig. 3. Dependence of broadband albedos on (A) SZA and (B) atmospheric visibility with the fixed surface reflectance spectra of snow and deciduous forest. All simulations were based on 1976 U.S. Standard atmosphere. Visibility value is (A) 25 km, and (B) SZA is 60°.

and atmospheric visibility value are very large, broadband albedos are relatively stable, which forms the foundation of this study. We can predict broadband albedos very well even when we do not know the atmospheric conditions. However, the diffuse and direct components are more sensitive to the atmospheric conditions. The uncertainties of predicting these separate components are usually much larger than total broadband albedo.

Fig. 4 presents the relationships between the total visible albedos and their separated direct and diffuse albedos, the total near-IR albedos and their separated direct and diffuse albedos, and the total shortwave albedo and the total visible/near-IR albedos. For snow and water surfaces, the total visible albedos are very close to both direct and diffuse visible albedos. For canopy and soil surfaces, however, diffuse visible albedos are smaller and direct visible albedos are larger than the total visible albedos.

For near-IR albedos, the relationships are much more complicated. In general, direct albedo is more sensitive to the variation of the atmospheric conditions and SZA. This can be well understood by examining Fig. 2 where diffuse

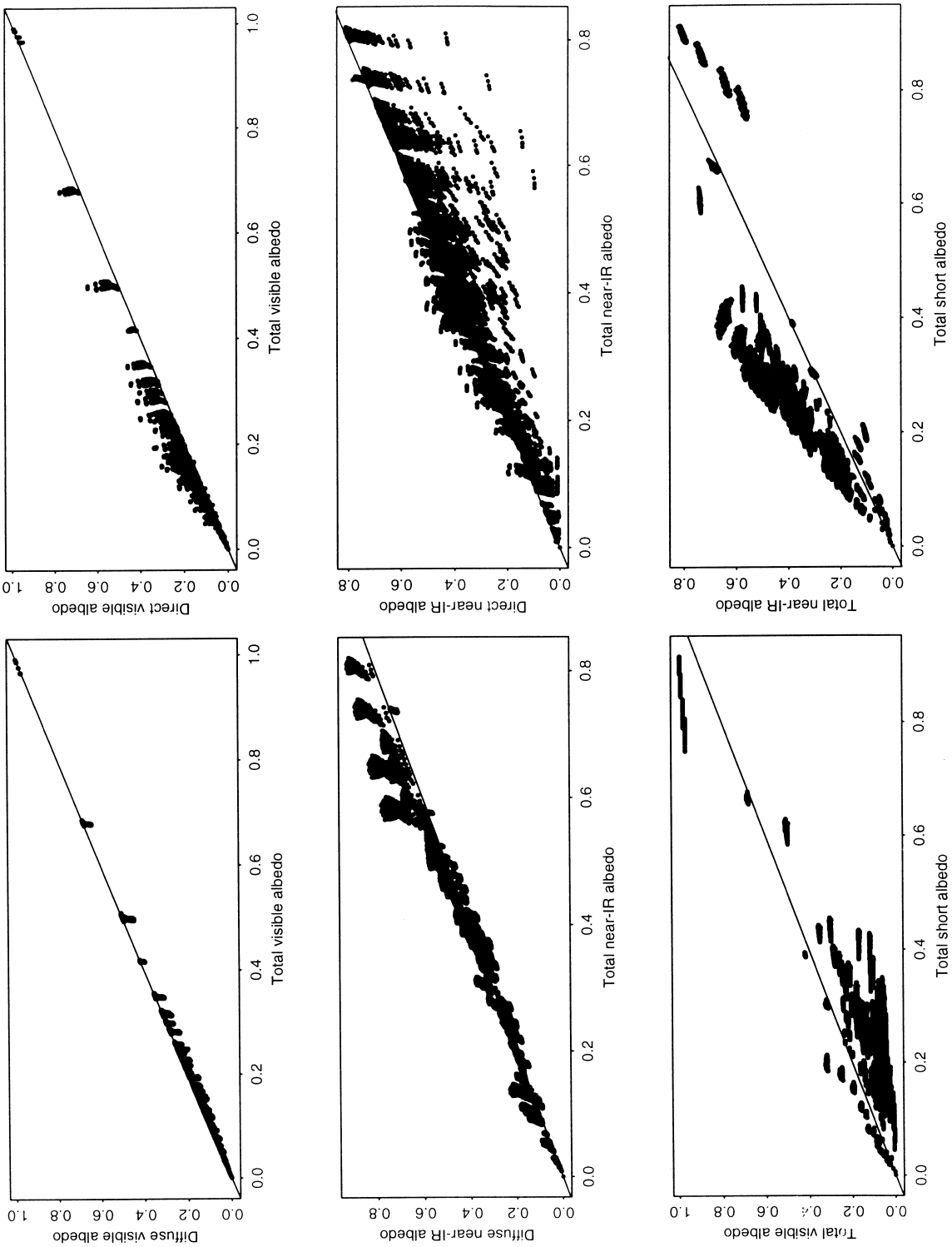

Fig. 4. Relationships between the total shortwave albedo and the total visible albedo and total near-IR albedo, total visible albedos and their separated direct and diffuse albedos, total near-IR albedos and their separated direct and diffuse components.

fluxes are reduced proportionally from visible to near-IR spectrum as the atmosphere varies from turbid to clear, but the direct fluxes increase much more in the visible spectrum than in the near-IR spectrum. Snow surfaces have much larger visible albedo and smaller near-IR albedo than the total shortwave albedo, canopy and soil surfaces have much smaller visible albedo and larger near-IR albedo than the total shortwave albedo. These observations are very consistent with our current understanding.

4. Conversion formulae

The formulae below are provided for the following sensors: Advanced Spaceborne Thermal Emission and Reflection Radiometer (ASTER), Advanced Very High Resolution Radiometer (AVHRR), Geostationary Operational Environmental Satellite (GOES). Landsat-7 Enhanced Thematic Mapper Plus (ETM+), Multiangle Imaging SpectroRadiometer (MISR), Moderate Resolution Imaging Spectroradiometer (MODIS), Polarization and Directionality of Earth's Reflectances (POLDER), and VEGETATION in SPOT spacecraft. Their spectral wavebands and wavelength ranges are specified in Table 1.

For the reflective spectral region, we provide conversion formulae for six broadband albedos: total visible albedo, diffuse and direct visible albedo, total near-IR albedo, and direct and diffuse near-IR albedos. Two parameters are used to measure the fitting: residual standard error (RSE) and multiple R-squared (R^2). Since our data sets have a wide range of albedos from dark water to snow, R^2 in the following fittings are very high in all the cases, and RSE is a better indicator of the fitting. The total number of samples in the regression analysis is 126,720 (256 surface types $\times$ 5 atmospheric profiles $\times$ 11 visibility values $\times$ 9 SZAs).

4.1. ASTER

ASTER is a research facility instrument provided by Japan on board the Terra satellite that was launched in December, 1999. It has three visible and near-IR bands with 15 m spatial resolution and six short IR bands with 30 m spatial resolution (see Table 1) and five thermal bands. The primary scientific objective of the ASTER mission is to improve understanding of the local- and regional-scale processes occurring on or near the earth's surface and lower atmosphere (Yamaguchi et al., 1998). For consistency, we denote bands in 0.4–0.7 μm as the visible bands, and bands in 0.7–2.5 μm as the near-IR bands in the rest of the paper.

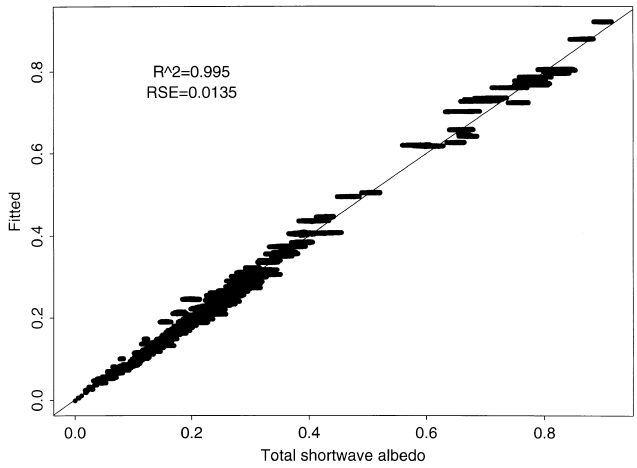

Fig. 5. Simulated total shortwave albedo and predicted by ASTER narrowband albedos.

ASTER has nine bands. It is expected that so many bands should enable us to convert narrowband to broadband albedos effectively. We found that the conversions are quite linear. The simulated broadband albedos and the fitted ones are displayed in Figs. 5 and 6, the summaries of the fitted residuals are presented in Table 2. The resultant linear equations are collated in Eq. (4)

$$\alpha_{\text{short}} = 0.484\alpha_1 + 0.335\alpha_3 - 0.324\alpha_5 + 0.551\alpha_6 + 0.305\alpha_8 - 0.367\alpha_9 - 0.0015$$

$$\alpha_{\text{visible}} = 0.820\alpha_1 + 0.183\alpha_2 - 0.034\alpha_3 - 0.085\alpha_4 - 0.298\alpha_5 + 0.352\alpha_6 + 0.239\alpha_7 - 0.240\alpha_9 - 0.001$$

Table 1
Spectral bands of the narrowband sensors

	Spectral bands and their wavelength ranges (μm)								
Sensors	1	2	3	4	5	6	7	8	9
ASTER	0.52–0.6	0.63–0.69	0.78–0.86	1.6–1.7	2.15–2.18	2.18–2.22	2.23–2.28	2.29–2.36	2.36–2.43
AVHRR-14	0.57–0.71	0.72–1.01	–	–	–	–	–	–	–
GOES-8	0.52–0.72	–	–	–	–	–	–	–	–
ETM+	0.45–0.51	0.52–0.6	0.63–0.69	0.75–0.9	1.55–1.75	–	2.09–2.35	–	–
MISR	0.42–0.45	0.54–0.55	0.66–0.67	0.85–0.87	–	–	–	–	–
MODIS	0.62–0.67	0.84–0.87	0.46–0.48	0.54–0.56	1.23–1.25	1.63–1.65	2.11–2.15	–	–
POLDER	0.43–0.46	0.66–0.68	0.74–0.79	0.84–0.88	–	–	–	–	–
VEGETATION	0.43–0.47	0.61–0.68	0.78–0.89	1.58–1.75	–	–	–	–	–

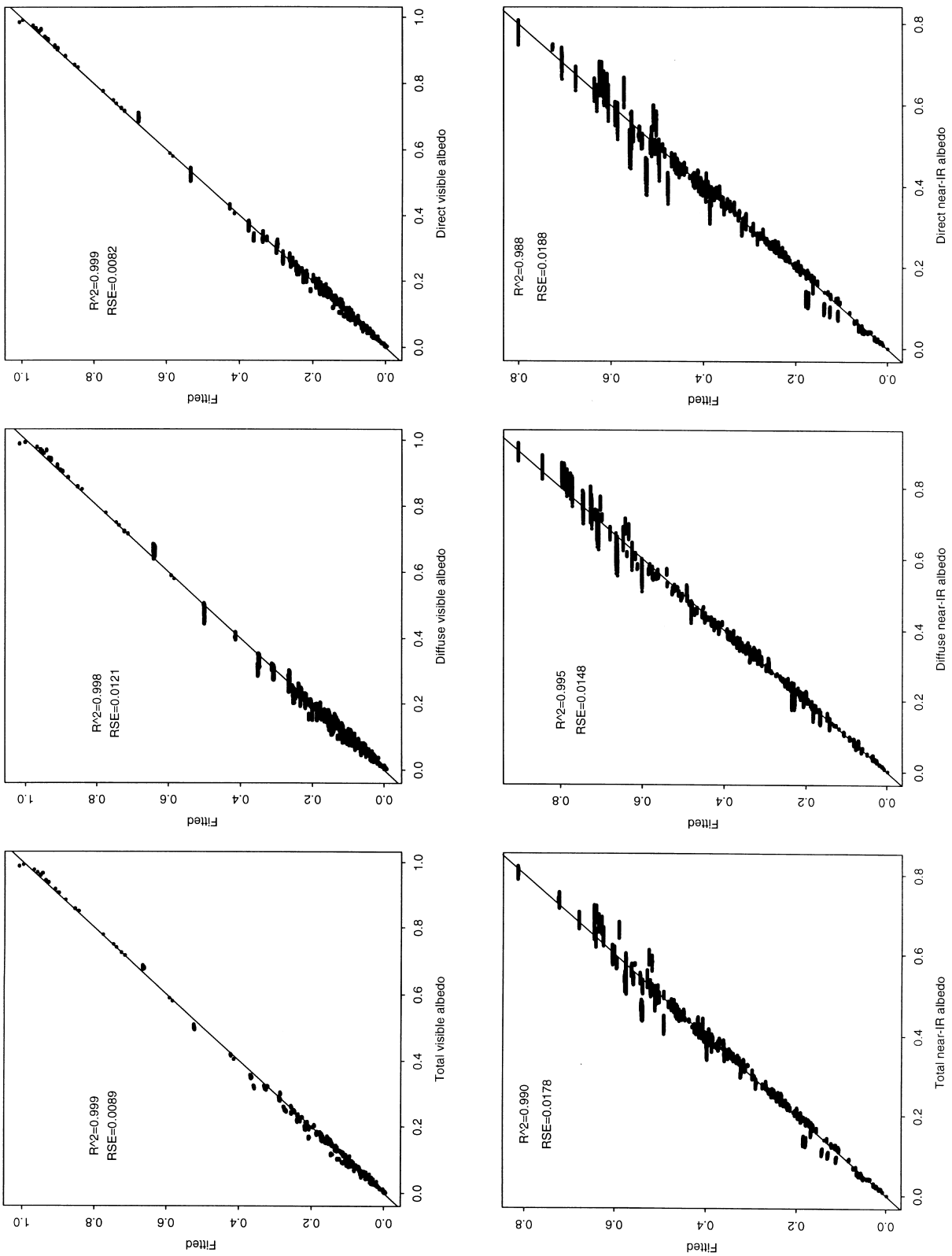

Fig. 6. Simulated broadband visible and near-IR albedos (total, direct, and diffuse) and predicted by ASTER narrowband albedos.

Table 2
Summary of the ASTER fitting residuals

Albedo	Min	1Q	Median	3Q	Max
Shortwave	−0.07058	−0.00656	0.00038	0.00709	0.04922
Visible	−0.04495	−0.00323	0.00216	0.00502	0.02159
Diffuse-visible	−0.06872	−0.00413	0.00249	0.00696	0.04231
Direct-visible	−0.04058	−0.00272	0.00180	0.00463	0.03534
NIR	−0.1042	−0.00467	0.00087	0.00600	0.08971
Diffuse-NIR	−0.10890	−0.00490	0.00076	0.004596	0.07764
Direct-NIR	−0.14410	−0.00496	0.00097	0.00627	0.09489

$$\alpha_{\text{diffuse-visible}} = 0.911\alpha_1 + 0.089\alpha_2 - 0.040\alpha_3 - 0.109\alpha_4 - 0.388\alpha_5 + 0.441\alpha_6 + 0.316\alpha_7 - 0.303\alpha_9 - 0.002$$

$$\alpha_{\text{direct-visible}} = 0.781\alpha_1 + 0.224\alpha_2 - 0.032\alpha_3 - 0.070\alpha_4 - 0.257\alpha_5 + 0.308\alpha_6 + 0.200\alpha_7 - 0.208\alpha_9 - 0.001$$

$$\alpha_{\text{NIR}} = 0.654\alpha_3 + 0.262\alpha_4 - 0.391\alpha_5 + 0.500\alpha_6 - 0.002$$

$$\alpha_{\text{diffuse-NIR}} = 0.835\alpha_3 + 0.033\alpha_4 - 0.191\alpha_5 + 0.352\alpha_6 - 0.002$$

$$\alpha_{\text{direct-NIR}} = 0.629\alpha_3 + 0.295\alpha_4 - 0.418\alpha_5 + 0.517\alpha_6 - 0.001. \quad (4)$$

It is evident that not all of bands are necessary to calculate broadband albedos. For example, only six bands are needed to calculate the total shortwave albedo. For visible broadband albedos, the coefficients of eight bands are provided. We also tried to fit data using two visible bands, and the results are quite reasonable (Eq. (5)),

$$\alpha_{\text{visible}} = 0.8845\alpha_1 + 0.122\alpha_2 - 0.0158, \quad (5)$$

with R^2=.997, RSE = 0.01293, the maximum residual is $\varepsilon_{\max} = 0.01936$, and the minimum residual is $\varepsilon_{\min} = -0.07316$. For diffuse visible albedo, the fitting results are similar. However, the fitting of visible direct albedo is less satisfactory since it is more sensitive to the atmospheric conditions and SZA. We found that the largest residuals are associated with very low visibility (2 km) and very large SZA (80°). The coefficients for direct visible albedo were derived without using these samples. We also tried to use SZA as an independent variable, but it did not improve the fitting significantly.

For the total near-IR albedo, four near-IR bands produce almost the equivalent results to all nine visible and near-IR bands. But the maximum residual is near 0.1. The extreme residuals are almost the same when we excluded those samples associated with large SZA (80°) and low visibility (2 km) or incorporated SZA as an independent variable. It probably implies that the ASTER near-IR bands are not best located for distinguishing reflectivity of different cover types. For diffuse near-IR albedo, the same four near-IR bands are used. But the extreme residuals are larger. The coefficients did not change much when we excluded the large SZA (80°) and low visibility (2 km). It was difficult to fit a linear model to direct near-IR albedo well.

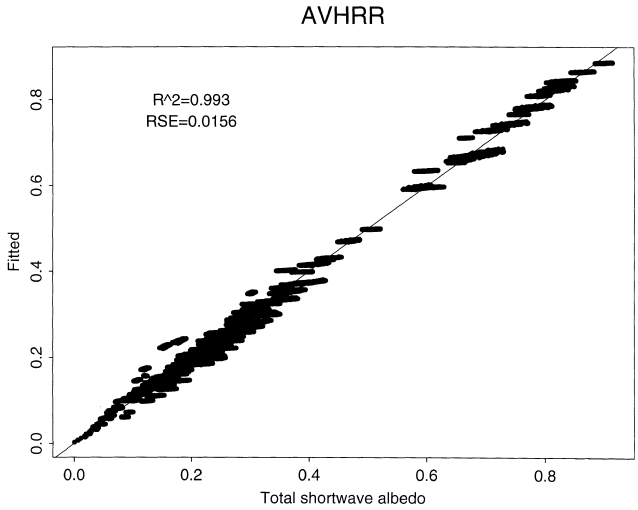

Fig. 7. Simulated total shortwave albedo and predicted by AVHRR narrowband albedos.

4.2. AVHRR

Data from AVHRR sensors have been acquired since 1981 and are expected to continue. They have been widely used for a variety of applications (Townshend, 1994), including the generation of the global albedo products (e.g., Csiszar & Gutman, 1999; Strugnell & Lucht, 2000). As mentioned in the Introduction, many studies have been reported to provide the AVHRR conversion formulae. Most studies were for either very bright surfaces (e.g., snow/ice) or low reflectance surfaces (soil/vegetation), and also suggested the linear conversions. Our experiments showed that the nonlinear fittings are much better than linear regression since AVHRR has only two bands that do not capture spectral variations of many different cover types very well. One approach is to separate cover types into snow, vegetation, soil, and so on (e.g., Brest & Goward, 1987; Song & Gao, 1999), which may introduce errors since the separation of these cover types is not trivial. Instead we make use of the high-order polynomial in this study.

For the total shortwave albedo, we explored to fit data using different orders of polynomial regression. The fitting is better as the order increases, but there are little improvements after the order is greater than two. The fitting of the total shortwave albedo using the second-order polynomial regression is presented in Fig. 7, and the resultant equation has the form (Eq. (6)):

$$\alpha_{\text{short}} = -0.3376\alpha_1^2 - 0.2707\alpha_2^2 + 0.7074\alpha_1\alpha_2 + 0.2915\alpha_1 + 0.5256\alpha_2 + 0.0035. \quad (6)$$

For visible and near-IR albedos, the fittings are shown in Fig. 8, and the equations are given by Eq. (7)

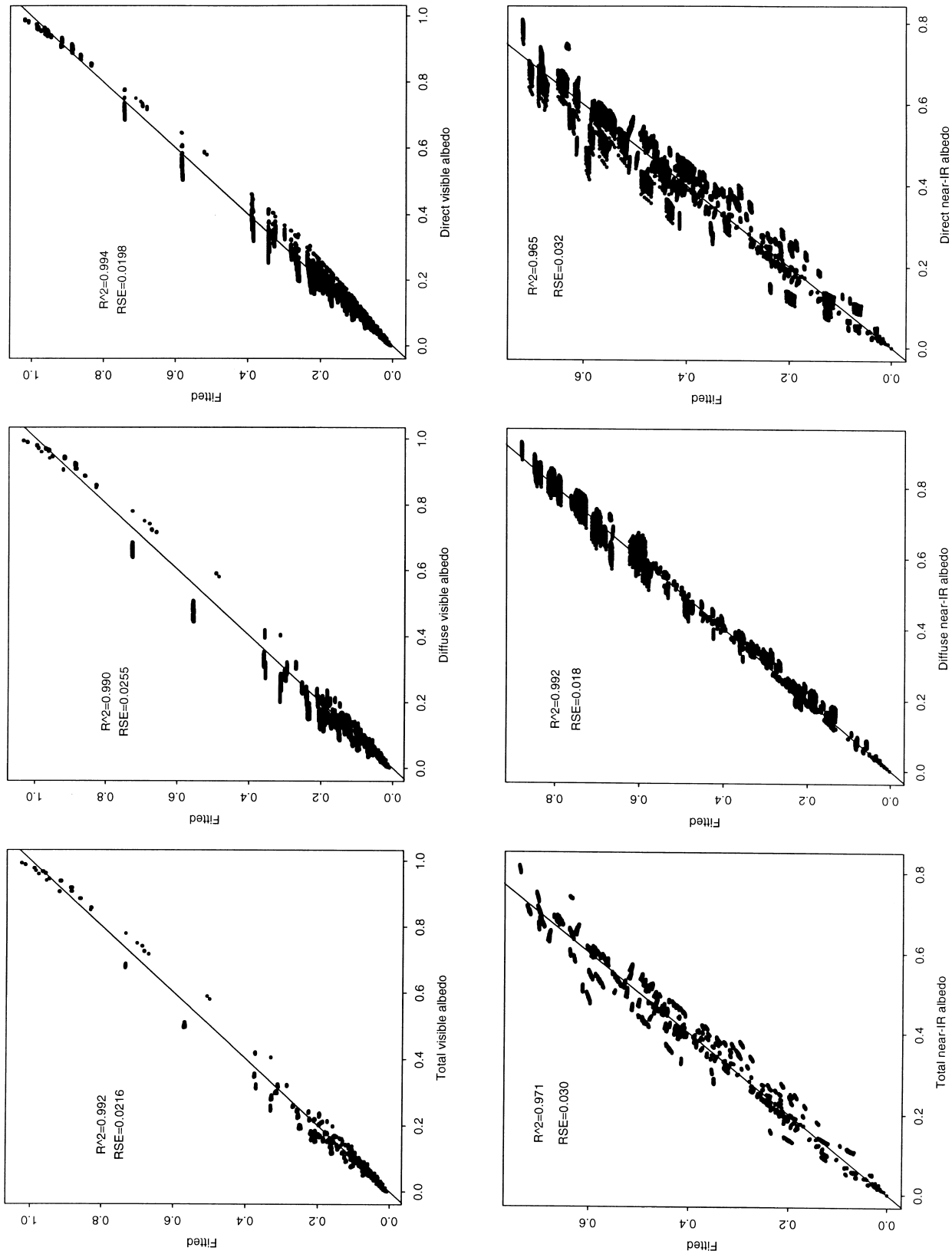

Fig. 8. Simulated broadband visible and near-IR albedos (total, direct, and diffuse) and predicted by AVHRR narrowband albedos.

$$\alpha_{visible} = 0.0074 + 0.5975\alpha_1 + 0.4410\alpha_1^2$$

$$\alpha_{diffuse-visible} = 0.0093 + 0.5190\alpha_1 + 0.5257\alpha_1^2$$

$$\alpha_{direct-visible} = 0.0051 + 0.6685\alpha_1 + 0.3648\alpha_1^2$$

$$\alpha_{NIR} = -1.4759\alpha_1^2 - 0.6536\alpha_2^2 + 1.8591\alpha_1\alpha_2 + 1.063\alpha_2$$

$$\alpha_{diffuse-NIR} = -0.628\alpha_1^2 - 0.3047\alpha_2^2 + 0.8476\alpha_1\alpha_2 + 1.0113\alpha_2 + 0.002$$

$$\alpha_{direct-NIR} = -1.5696\alpha_1^2 - 0.6961\alpha_2^2 + 1.9679\alpha_1\alpha_2 + 1.0708\alpha_2. \quad (7)$$

The summaries of the fitted residuals are presented in Table 3. Note that since direct near-IR albedo is very sensitive to the incoming downward flux, the above formula for calculating direct near-IR albedo was derived without utilizing samples with SZA 80° and atmospheric visibility 2 km. Otherwise, very large residuals were associated with these samples. Moreover, since direct flux is very small under such conditions, numerical errors may affect the fitting results.

Table 3
Summary of the AVHRR fitting residuals

Albedo	Min	1Q	Median	3Q	Max
Shortwave	− 0.07691	− 0.00856	0.00013	0.00951	0.05872
Visible	− 0.08671	− 0.00861	− 0.00025	0.01018	0.08099
Diffuse-visible	− 0.1148	− 0.01006	0.00009	0.01206	0.09647
Direct-visible	− 0.09315	− 0.00719	0.00021	0.009553	0.07696
NIR	− 0.1382	− 0.01645	− 0.00206	0.01984	0.1042
Diffuse-NIR	− 0.09733	− 0.00919	− 0.00155	0.00998	0.07132
Direct-NIR	− 0.175	− 0.01726	− 0.0021	0.0212	0.1175

The coefficients were derived based on NOAA14 AVHRR spectral response functions. We also experimented by using the AVHRR spectral response functions of NOAA7, 9, and 11, and found no significantly different results.

There are several studies on converting AVHRR narrowband albedos to the total shortwave broadband albedo (e.g., Key, 1996; Russell et al., 1997; Song & Gao, 1999; Stroeve et al., 1997; Valiente et al., 1995), most of which

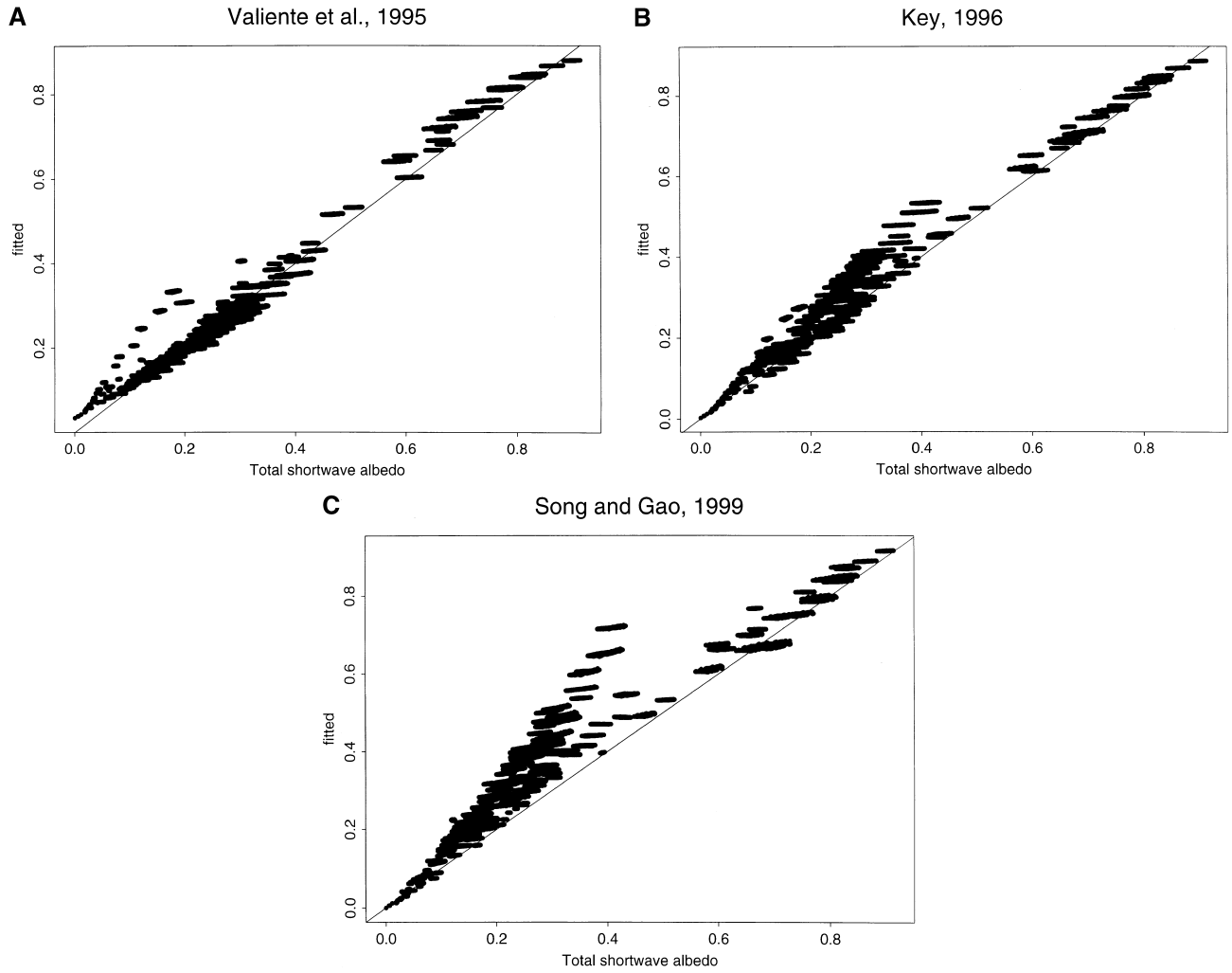

Fig. 9. Comparisons of the simulated total shortware albedo with the published AVHRR formulae by (A) Valiente et al. (1995), (B) Key (1996), and (C) Song and Gao (1999).

were based on experimental data with the limited number of surface types and atmospheric conditions. To verify our approach and results, we tested several formulae using our simulated database. Fig. 9 compares the simulated total shortwave albedo and the predicted ones by the formulae of Key (1996), Song and Gao (1999), and Valiente et al. (1995). Key's formula was primarily for snow/ice and does fit our snow/ice samples well, and also some vegetation, soil, wetland, and water samples. The formula of Valiente et al. fits most vegetation/soil samples very well, but overestimates water/wetland and snow samples, probably because of the fact they mainly used vegetation/soil reflectance spectra in their simulations. Song and Gao (1999) develop a linear conversion formula whose coefficients are the second-order polynomial functions of normalized difference vegetation index (NDVI, Eq. (8))

$$\alpha_{\text{short}} = (0.494\text{NDVI}^2 - 0.329\text{NDVI} + 0.372)\alpha_1 + (-1.439\text{NDVI}^2 + 1.209\text{NDVI} + 0.587)\alpha_2. \quad (8)$$

Their formula overestimates the total shortwave albedo of most vegetation and soil samples, but fits low and very high albedos very well. It is probably because their formula was derived from ground measurements with the limited atmospheric and surface conditions.

4.3. GOES

Geostationary Operational Environmental Satellite (GOES) has been commissioned and operated by NOAA. Normally there are two GOES satellites in operation. GOES-East is stationed at 75° and GOES-West at 135° west. These provide coverage of most of the Western Hemisphere. GOES has five imagers, but only one band is in the shortwave reflective region. This one-band image has been widely used to provide surface broadband albedo products (e.g., Pinker, Kustas, Laszlo, Moran, & Huete, 1994; Pinker, Frouin, & Li, 1995). As we will demonstrate below, one band cannot adequately capture the variation of surface reflective properties, and therefore the accuracy of the GOES broadband albedo products is very questionable.

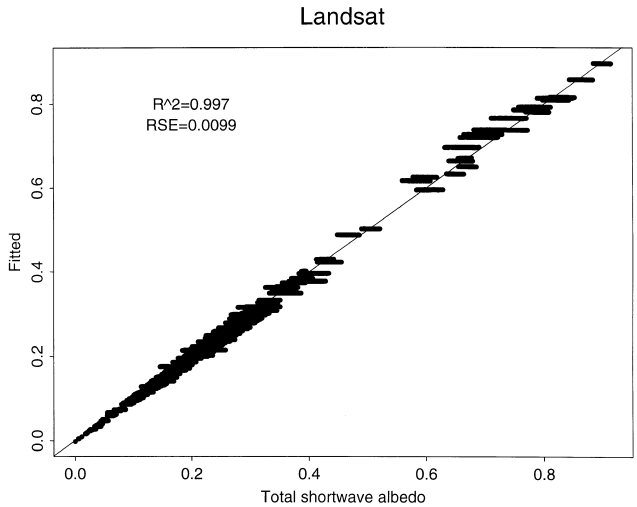

Fig. 10. Simulated total shortwave albedo and predicted by ETM+/TM narrowband albedos.

Table 4
Summary of the GOES fitting residuals

Albedo	Min	1Q	Median	3Q	Max
Shortwave	−0.1846	−0.03012	−0.00034	0.03053	0.1575
Visible	−0.08102	−0.01526	−0.00024	0.01501	0.07042
Diffuse-visible	−0.09677	−0.01508	−0.00149	0.01617	0.08546
Direct-visible	−0.09682	−0.01471	0.00132	0.01592	0.1131

For total shortwave albedo, the conversion formula (Eq. (9)) is

$$\alpha_{\text{short}} = 0.0759 + 0.7712\alpha. \quad (9)$$

For visible albedos, a 2nd-order polynomial function can produce good fits (Eq. (10)):

$$\alpha_{\text{visible}} = -0.0084 + 0.689\alpha + 0.3604\alpha^2$$

$$\alpha_{\text{diffuse-visible}} = -0.006 + 0.6119\alpha + 0.443\alpha^2$$

$$\alpha_{\text{direct-visible}} = -0.0111 + 0.7586\alpha + 0.2862\alpha^2. \quad (10)$$

The fitted results are displayed in Fig. 10 and summarized in Table 4. Note that these fitting results were obtained from data of all SZAs and all visibility values.

The near-IR broadband albedo cannot be predicted by one GOES band albedo simply because the spectral coverage of the band is mainly on the visible spectrum. This also explains why one GOES band cannot predict total shortwave albedo.

We used both GOES8 and GOES10 sensor spectral response functions and the results are almost identical.

4.4. Landsat TM/ETM+

Landsat Thematic Mapper (TM) started to acquire imagery in 1982 boarded on Landsat-4 and -5. Landsat-7 was launched in April 1999 and carries the enhanced thematic mapper plus (ETM+). Both ETM+ and TM have the same multispectral reflective wavebands with the similar spectral coverages. They have produced repetitive and high-resolution multispectral imagery of the earth's land surface globally.

The earlier studies on calculating the total shortwave broadband albedo from Landsat narrowbands (e.g., Brest & Goward, 1987) primarily relied on the relations between TOA reflectances and ground measured broadband albedo. Since it is now practical to retrieve surface

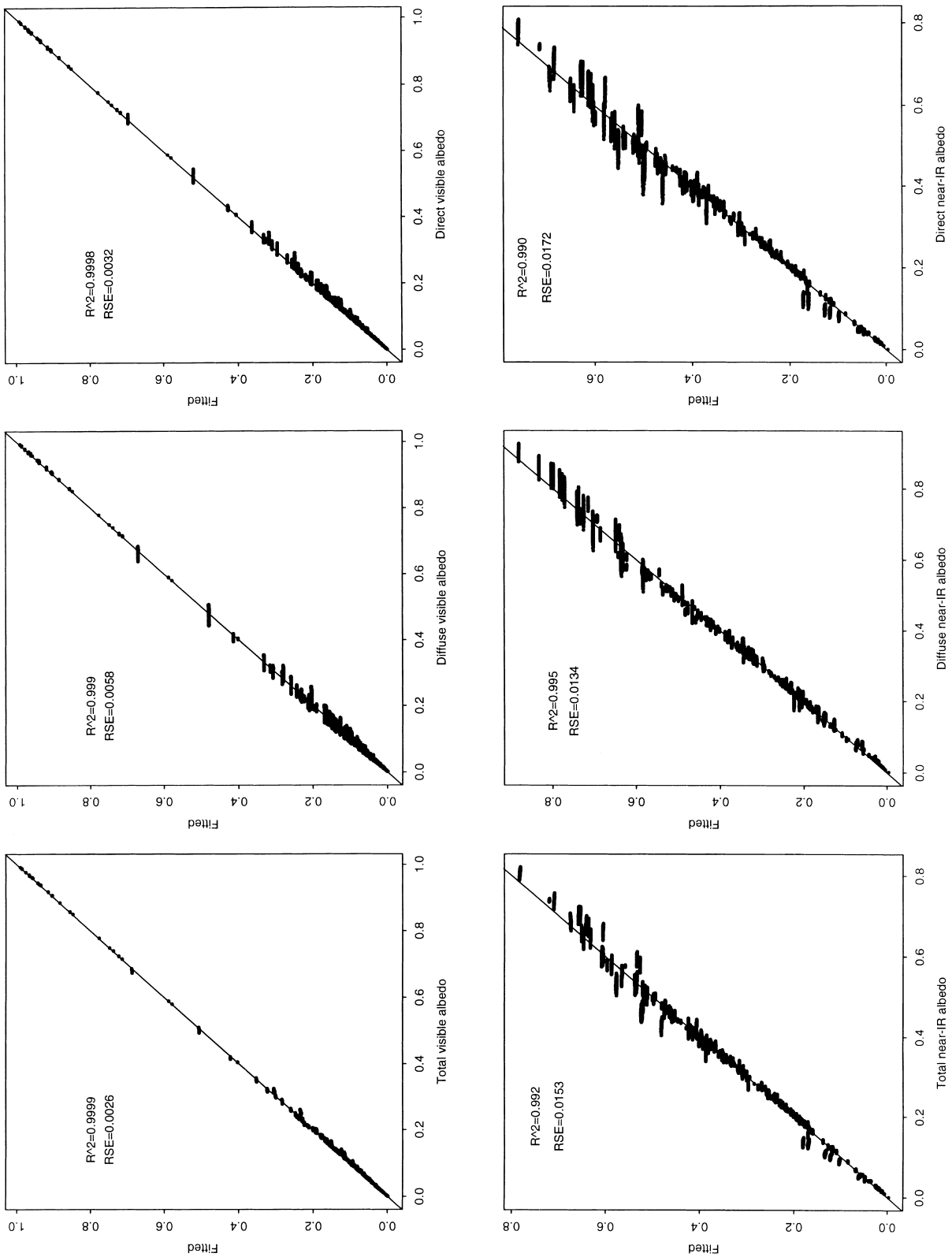

Fig. 11. Simulated broadband visible and near-IR albedos (total, direct, and diffuse) and predicted by ETM+/TM narrowband albedos.

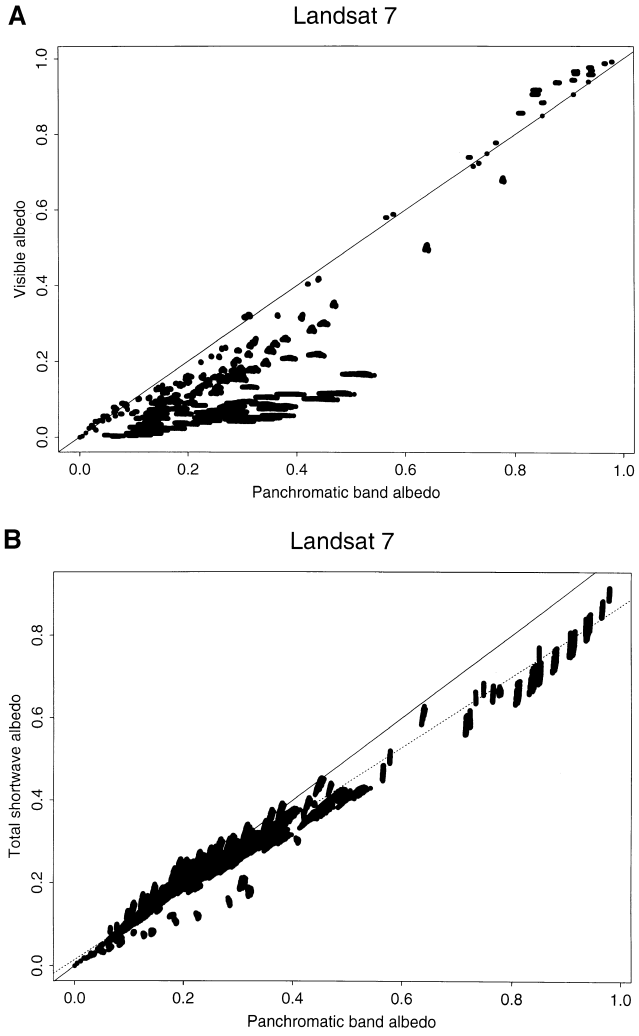

Fig. 12. Relations between ETM+ panchromatic band albedo and (A) total visible and (B) shortwave albedos.

spectral reflectance by performing the atmospheric correction procedure (e.g., Liang et al., 1997), the equations presented in this study are only suitable for surface spectral albedos.

When we tried to use all six bands to predict the total shortwave albedo, the standard deviation of the band2 coefficient was too big. After removing this band, RSE and R^2 were not significantly changed. It is therefore suggested to use five bands for predicting the total shortwave albedo. The fitting results are displayed in Figs. 11 and 12, the summaries of the fitted residuals are presented in Table 5. The linear equations are given by

$$\alpha_{\text{short}} = 0.356\alpha_1 + 0.130\alpha_3 + 0.373\alpha_4 + 0.085\alpha_5 + 0.072\alpha_7 - 0.0018$$

$$\alpha_{\text{visible}} = 0.443\alpha_1 + 0.317\alpha_2 + 0.240\alpha_3$$

$$\alpha_{\text{diffuse-visible}} = 0.556\alpha_1 + 0.281\alpha_2 + 0.163\alpha_3 - 0.0014$$

Table 5
Summary of the LANDSAT fitting residuals

Albedo	Min	1Q	Median	3Q	Max
Shortwave	−0.06436	−0.00497	−0.00015	0.00465	0.05018
Visible	−0.01333	−0.00112	0.00024	0.0009	0.02461
Diffuse-visible	−0.03731	−0.00186	0.00064	0.00191	0.05097
Direct-visible	−0.01638	−0.00124	0.00019	0.00084	0.04361
NIR	−0.08793	−0.00395	0.00107	0.00491	0.07855
Diffuse-NIR	−0.0824	−0.0056	0.00014	0.00484	0.07139
Direct-NIR	−0.1214	−0.00426	0.00141	0.0043	0.09101

$$\alpha_{\text{direct-visible}} = 0.390\alpha_1 + 0.337\alpha_2 + 0.274\alpha_3$$

$$\alpha_{\text{NIR}} = 0.693\alpha_4 + 0.212\alpha_5 + 0.116\alpha_7 - 0.003$$

$$\alpha_{\text{diffuse-NIR}} = 0.864\alpha_4 + 0.158\alpha_7 - 0.0043$$

$$\alpha_{\text{direct-NIR}} = 0.659\alpha_4 + 0.342\alpha_5 - 0.0033. \quad (11)$$

For visible albedos, three visible bands are sufficient to predict broadband albedos very well. Although the residuals are a little bit larger for direct visible albedo, they

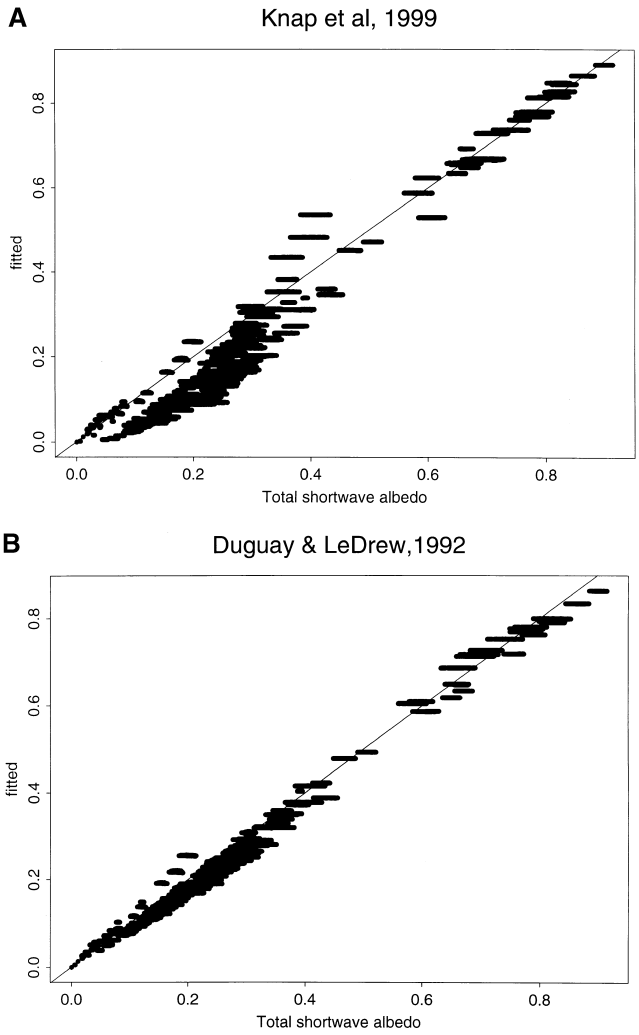

Fig. 13. Comparisons with published TM formulae by (A) Knap et al. (1999) and (B) Duguay and LeDrew (1992).

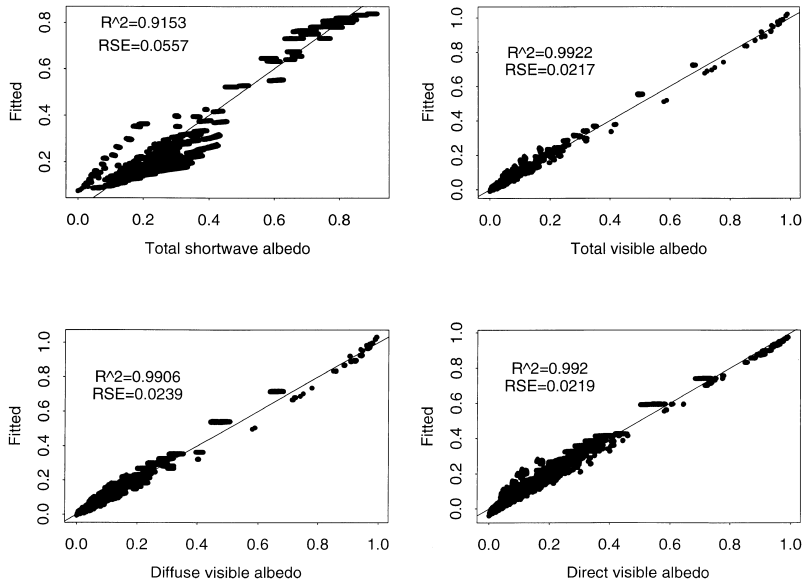

Fig. 14. Simulated total shortwave and visible albedos and predicted by GOES visible imager.

are associated with very low visibility and large SZA. When we excluded samples of large SZA (80°) and low visibility (2 km), the maximum residual was drooped to 0.0436, and the minimum residuals was dropped to -0.01638. When we tried to incorporate ETM+ panchromatic band, the fittings did not improve significantly. Fig. 13 displays the relations between panchromatic band albedo and the total visible/shortwave albedos. It is clear that visible albedo is smaller for most soil and vegetation samples and larger for snow and ice surfaces. It is because ETM+ panchromatic band is much wider than the visible band and contains information in the near-IR spectrum in which soil and vegetation have much larger albedos. On the other hand, panchromatic band albedo is a better indicator of the total shortwave albedo. In this figure, the dashed line represents a linear fitting, $\alpha_{short} = 0.8558\alpha_{pan} + 0.015$, with R^2=.986, RSE = 0.0226, the minimum and maximum residuals are -0.121 and 0.076, respectively.

For near-IR broadband albedos, visible narrowbands did not help much. We therefore suggest using three near-IR bands. The fitting errors are larger than those in fitting visible albedos. As before, the fitting coefficients for direct near-IR albedo were obtained without using samples of large SZA (80°) and low visibility (2 km).

We also found that the coefficients are not sensitive to the spectral response functions of different Landsat TM sensors. In other words, the Eq. (11) are equally suitable for Landsat 4 and 5 TM imagery.

Few studies have been reported in the literature to derive surface broadband shortwave albedo from Landsat TM imagery (e.g., Brest & Goward, 1987; Duguay & LeDrew, 1992; Gratton, Howart, & Marceau, 1993; Knap, Reijmer, & Oerlemans, 1999). Knap et al. (1999) developed a second-order polynomial formula based on ground measurements of both glacier ice and snow (Eq. (12)):

$$\alpha_{short} = 0.726\alpha_2 - 0.322\alpha_2^2 - 0.051\alpha_4 + 0.581\alpha_4^2. \quad (12)$$

From Fig. 14, we can see that their formula fits our snow/ice samples quite well, but fits the soil/vegetation samples very poorly. Duguay and LeDrew (1992) developed a linear formula using three TM bands (Eq. (13)):

$$\alpha_{short} = 0.526\alpha_2 + 0.3139\alpha_4 + 0.112\alpha_7, \quad (13)$$

and it fits our data of all cover types surprisingly well.

Although we do not have ground measurements to validate our formulae at this point, comparisons with these

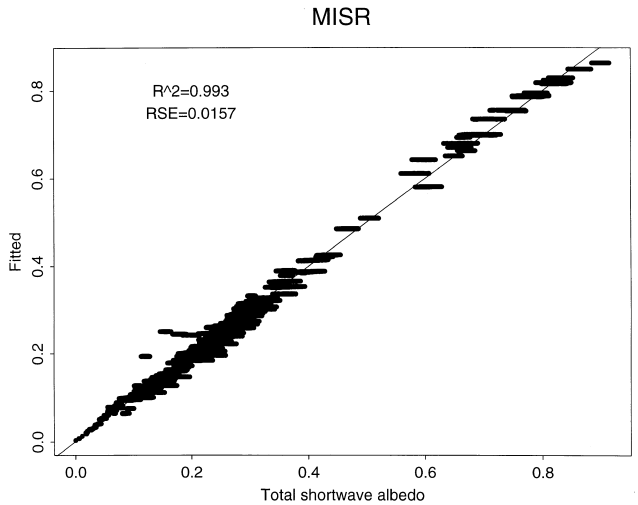

Fig. 15. Simulated total shortwave albedo and predicted by MISR narrowband albedos.

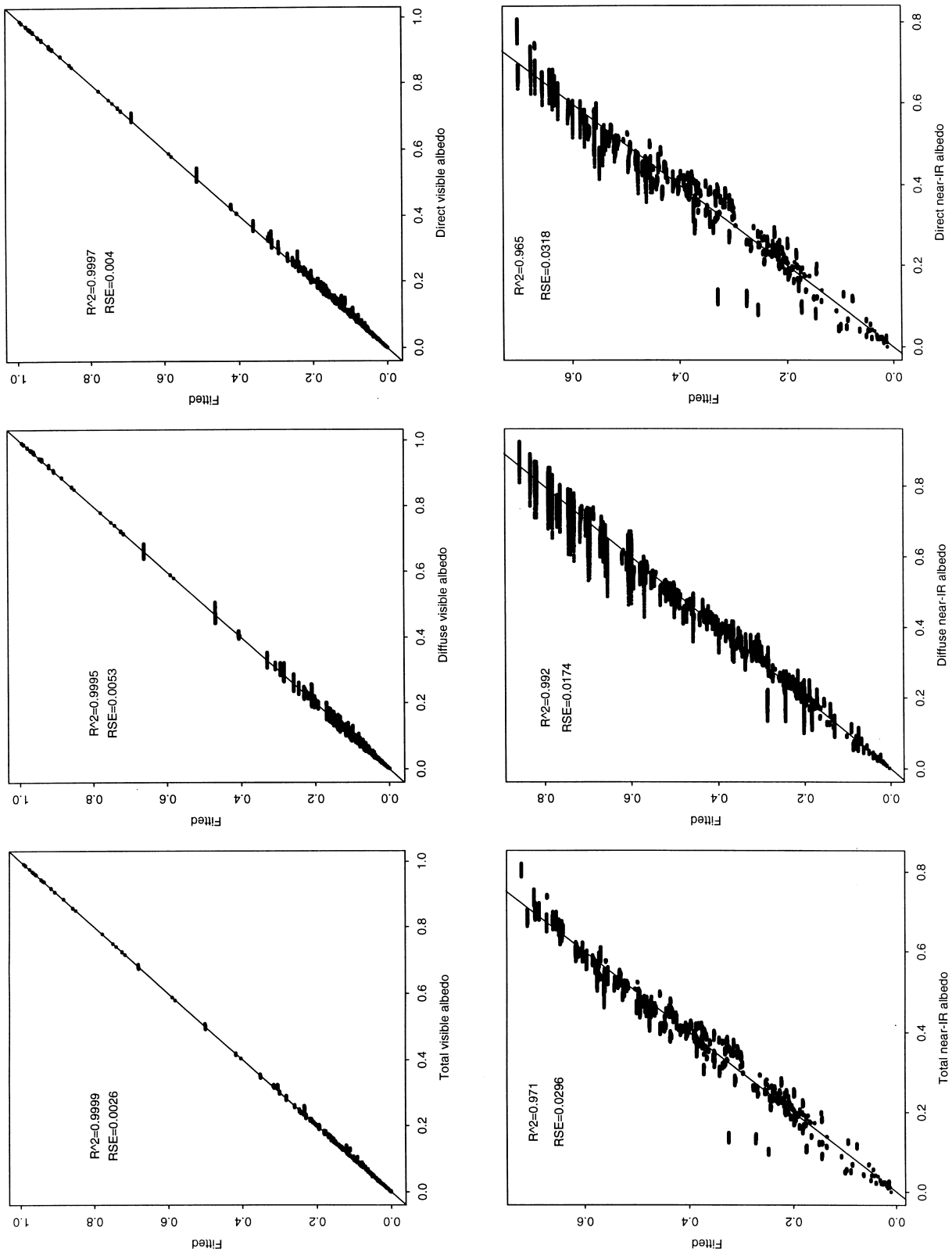

Fig. 16. Simulated broadband visible and near-IR albedos (total, direct, and diffuse) and predicted by MISR narrowband albedos.

Table 6
Summary of the MISR fitting residuals

Albedo	Min	1Q	Median	3Q	Max
Shortwave	−0.1045	−0.00687	0.00044	0.0083	0.06147
Visible	−0.00745	−0.00152	−0.00037	0.00058	0.0281
Diffuse-visible	−0.02603	−0.00184	−0.00006	0.00151	0.04695
Direct-visible	−0.01235	−0.0018	−0.00048	0.00084	0.04969
NIR	−0.2013	−0.013	0.00066	0.01743	0.09974
Diffuse-NIR	−0.1673	−0.00665	0.00084	0.00852	0.07176
Direct-NIR	−0.2258	−0.01385	0.00078	0.01869	0.1085

published formulae in the literature provide a sufficient amount of evidence indicating that our data sets are reliable and the formulae derived from them are reasonable.

4.5. MISR

The MISR instrument is designed to improve our understanding of the earth's ecology, environment and climate (Diner et al., 1998). MISR images the earth in nine different view directions (one nadir view, and four off-nadir views pointing to each forward and backward direction) to infer the angular variation of reflected solar radiation within four spectral bands in the visible and near-IR spectrum. It takes 7 min for a point on the earth to be observed at all nine angles. It is carried by the Earth Observing System (EOS) spacecraft, Terra, that was launched in December 1999.

The linear conversion formulae are given by

$$\alpha_{\text{short}} = 0.126\alpha_2 + 0.343\alpha_3 + 0.415\alpha_4 + 0.0037$$

$$\alpha_{\text{visible}} = 0.381\alpha_1 + 0.334\alpha_2 + 0.287\alpha_3$$

$$\alpha_{\text{diffuse-visible}} = 0.478\alpha_1 + 0.306\alpha_2 + 0.219\alpha_3 - 0.001$$

$$\alpha_{\text{direct-visible}} = 0.335\alpha_1 + 0.349\alpha_2 + 0.317\alpha_3$$

$$\alpha_{\text{NIR}} = -0.387\alpha_1 - 0.196\alpha_2 + 0.504\alpha_3 + 0.830\alpha_4 + 0.011$$

$$\alpha_{\text{diffuse-NIR}} = -0.240\alpha_1 + 0.269\alpha_3 + 0.866\alpha_4 + 0.003$$

$$\alpha_{\text{direct-NIR}} = -0.407\alpha_1 - 0.226\alpha_2 + 0.536\alpha_3 + 0.826\alpha_4 + 0.012. \quad (14)$$

The fitting results for the total shortwave albedo are not bad (Fig. 15) considering MISR has only four bands in the visible and near-IR spectrum. For total and diffuse visible albedos (Fig. 16), the fittings are excellent with three visible bands. The fitting for direct visible albedo is also good, although the maximum residual is as large as 0.15. The summaries of the fitted residuals are presented in Table 6.

The MISR science team will generate the total visible albedo as their standard product (Diner et al., 1998). Conversion formulae for the total visible albedo in Eq. (14) can be used at least for the reference and cross comparison. The MISR team does not produce near-IR and total shortwave broadband albedos.

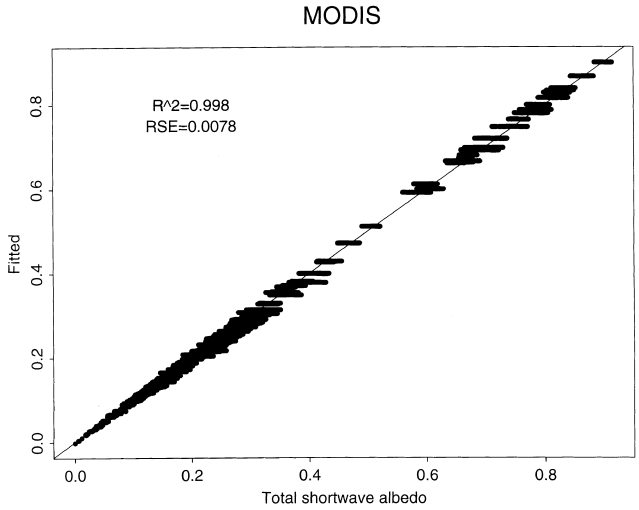

Fig. 17. Simulated total shortwave albedo and predicted by MODIS narrowband albedos.

Since MISR has only one band in the near-IR spectrum, the fitting for the near-IR is not good if we use only near-IR narrowband albedo. When all four bands are used, the predictions are much improved, but large scatters (residuals) do exist. We need to be very cautious about the accuracy requirements if we want to predict near-IR albedos using MISR narrowband albedos.

4.6. MODIS

MODIS is an EOS facility instrument designed to measure biological and physical processes on a global basis every 1-to-2 days, and will provide long-term observations from which an enhanced knowledge of global dynamics and processes occurring on the surface of the earth and in the lower atmosphere can be derived (King & Greenstone, 1999). It has been carried by Terra since December 1999 and will also be launched on Aqua in summer 2001. The MODIS science team will produce surface narrowband spectral albedos as well as three broadband (visible, near-IR, and shortwave) albedos (Lucht et al., 2000).

The fitting results are displayed in Figs. 17 and 18, and the summaries of the fitted residuals are presented in Table 7. the conversion formulae are given by Eq. (15):

$$\alpha_{\text{short}} = 0.160\alpha_1 + 0.291\alpha_2 + 0.243\alpha_3 + 0.116\alpha_4 + 0.112\alpha_5 + 0.081\alpha_7 - 0.0015$$

$$\alpha_{\text{visible}} = 0.331\alpha_1 + 0.424\alpha_3 + 0.246\alpha_4$$

$$\alpha_{\text{diffuse-visible}} = 0.246\alpha_1 + 0.528\alpha_3 + 0.226\alpha_4 - 0.0013$$

$$\alpha_{\text{direct-visible}} = 0.369\alpha_1 + 0.374\alpha_3 + 0.257\alpha_4$$

$$\alpha_{\text{NIR}} = 0.039\alpha_1 + 0.504\alpha_2 - 0.071\alpha_3 + 0.105\alpha_4 + 0.252\alpha_5 + 0.069\alpha_6 + 0.101\alpha_7$$

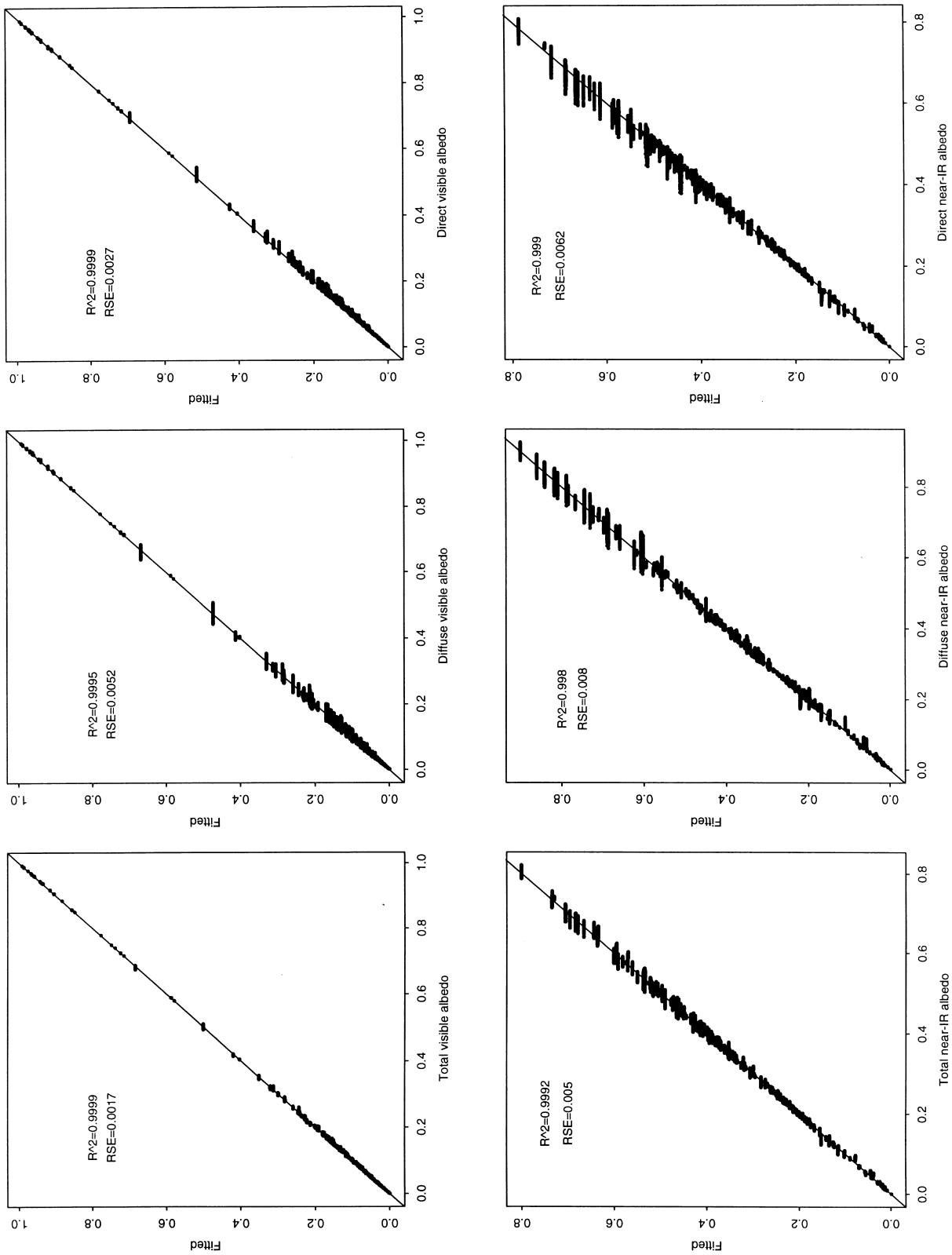

Fig. 18. Simulated broadband visible and near-IR albedos (total, direct, and diffuse) and predicted by MODIS narrowband albedos.

Table 7
Summary of the MODIS fitting residuals

Albedo	Min	1Q	Median	3Q	Max
Shortwave	−0.0376	−0.00446	−0.00059	0.00361	0.04876
Visible	−0.01064	−0.00071	0.00002	0.00065	0.01646
Diffuse-visible	−0.03075	−0.00161	0.00042	0.00164	0.04274
Direct-visible	−0.01102	−0.00106	0.000002	0.00065	0.03433
NIR	−0.03279	−0.00203	−0.00022	0.00187	0.03255
Diffuse-NIR	−0.06141	−0.00368	−0.00051	0.0031	0.066
Direct-NIR	−0.06997	−0.0021	−0.00017	0.00202	0.03658

$$\alpha_{\text{diffuse-NIR}} = 0.085\alpha_1 + 0.693\alpha_2 - 0.146\alpha_3 + 0.176\alpha_4 + 0.146\alpha_5 + 0.043\alpha_7 - 0.0021$$

$$\alpha_{\text{direct-NIR}} = 0.037\alpha_1 + 0.479\alpha_2 - 0.068\alpha_3 + 0.0976\alpha_4 + 0.266\alpha_5 + 0.0757\alpha_6 + 0.107\alpha_7. \quad (15)$$

MODIS's seven bands are excellent in making the broadband albedo conversions. The total shortwave albedo is calculated by using all seven bands, but visible albedos using three visible bands. All fittings look excellent.

For the total near-IR albedo, four near-IR narrowband albedos are very good predictors. However, when all seven bands are used, the fitting is significantly better. For diffuse near-IR albedo, three additional visible bands did not help much. Thus, only four bands are used. For direct near-IR albedo, all bands are used excluding samples with low visibility (2 km) and the large SZA (80°).

Note that in our previous study (Liang et al., 1999), we presented a set of coefficients for converting MODIS and MISR narrowband albedos to broadband inherent albedos that need to be converted to apparent albedos for various applications. The MODIS conversion formulae have been adopted for the generation of surface broadband albedos (Lucht et al., 2000). Here we convert them into average broadband apparent albedos under the general atmospheric conditions.

4.7. POLDER

The POLDER instrument (Deschamps et al., 1994) aboard the Japanese platform ADvanced Earth Observation Satellite (ADEOS) acquired measurements between November 1996 and June 1997. It will be carried again by ADEOS-2, which will be launched in 2001. The multi-directionality of the POLDER measurements (12–14 directions), coupled with POLDER information on aerosol and water vapor offers a unique opportunity to characterize the land surface albedo. Land surface spectral albedos will be provided as the standard products, but we need to convert them into broadband albedos in land surface modeling and applications. Hopefully, the conversion coefficients in this study will help extend the applications of the POLDER surface products.

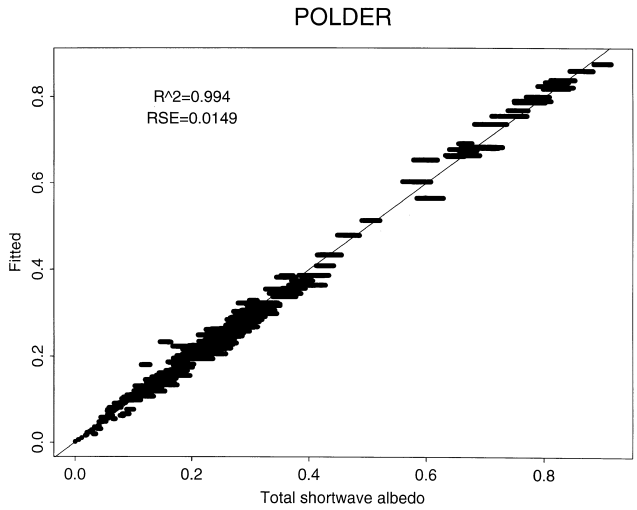

Fig. 19. Simulated total shortwave albedo and predicted by POLDER narrowband albedos.

The fitting results are shown in Figs. 19 and 20, and the summaries of the fitted residuals are presented in Table 8. The conversion formulae are given by Eq. (16)

$$\alpha_{\text{short}} = 0.112\alpha_1 + 0.388\alpha_2 - 0.266\alpha_3 + 0.668\alpha_4 + 0.0019$$

$$\alpha_{\text{visible}} = 0.533\alpha_1 + 0.412\alpha_2 + 0.215\alpha_3 - 0.168\alpha_4 + 0.0046$$

$$\alpha_{\text{diffuse-visible}} = 0.615\alpha_1 + 0.335\alpha_2 + 0.196\alpha_3 - 0.153\alpha_4 + 0.0036$$

$$\alpha_{\text{direct-visible}} = 0.495\alpha_1 + 0.447\alpha_2 + 0.223\alpha_3 - 0.175\alpha_4$$

$$\alpha_{\text{NIR}} = -0.397\alpha_1 + 0.451\alpha_2 - 0.756\alpha_3 + 1.498\alpha_4 + 0.0013$$

$$\alpha_{\text{diffuse-NIR}} = -0.209\alpha_1 + 0.279\alpha_2 - 0.210\alpha_3 + 1.045\alpha_4$$

$$\alpha_{\text{direct-NIR}} = -0.425\alpha_1 + 0.474\alpha_2 - 0.825\alpha_3 + 1.554\alpha_4 + 0.0018. \quad (16)$$

For the total shortwave albedo, the fitting is very good. For visible albedos, we recommend using all four bands. For near-IR bands, the linear fitting is not too good. POLDER has the same number of bands as MISR. Although they are located differently, their fittings look very similar.

4.8. VEGETATION

The VEGETATION program was developed jointly by France, the European Commission, Belgium, Italy, and Sweden. It is on board SPOT-4 that was launched last March 24, 1998. It has four spectral bands (see Table 1), and the spatial resolution is about 1 km at nadir. There is at least one observation daily acquired at 10:30 local solar time for latitude higher than 32°. The overall

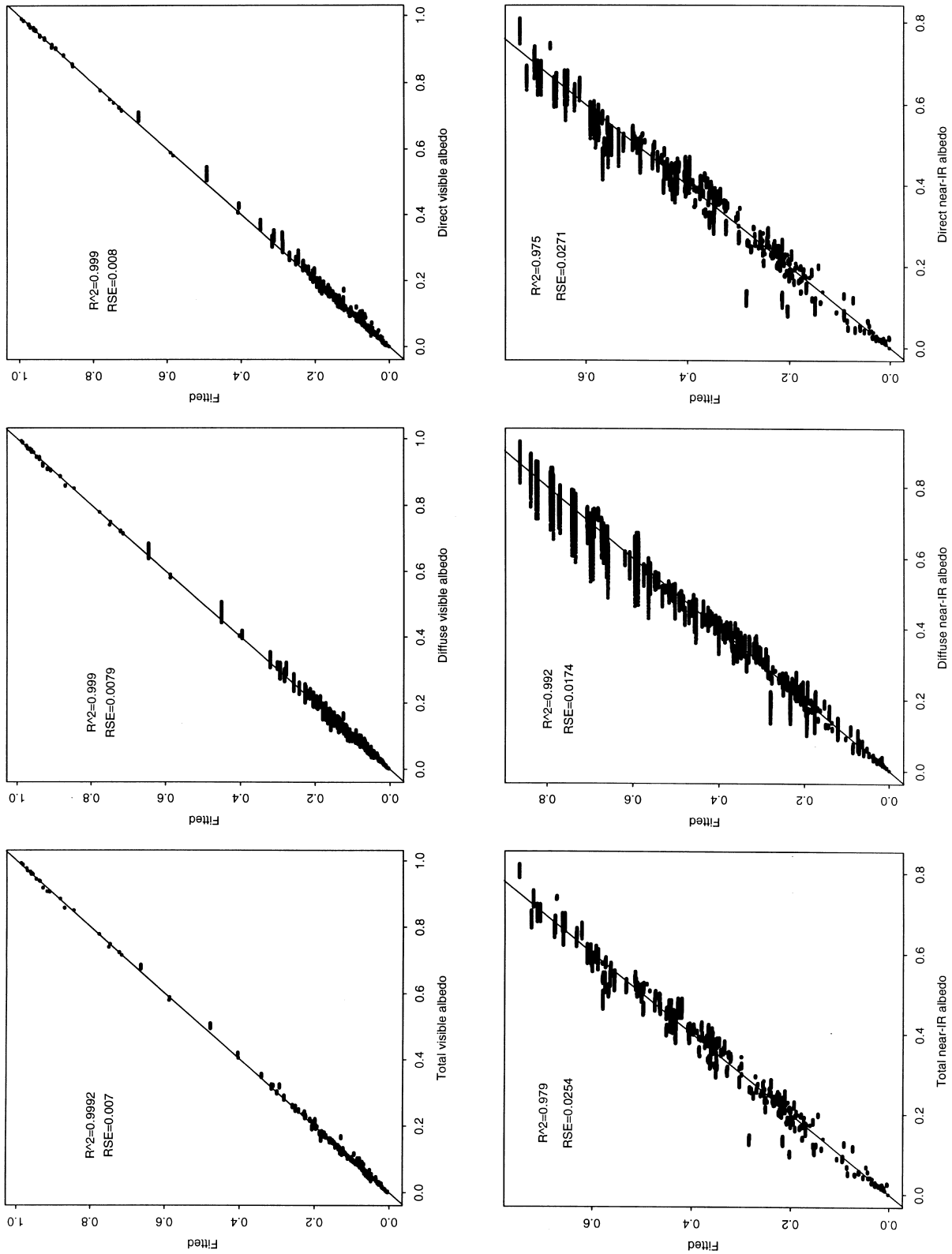

Fig. 20. Simulated broadband visible and near-IR albedos (total, direct, and diffuse) and predicted by POLDER narrowband albedos.

Table 8
Summary of the POLDER fitting residuals

Albedo	Min	1Q	Median	3Q	Max
Shortwave	−0.08737	−0.00827	0.00073	0.00868	0.06398
Visible	−0.02847	−0.00343	−0.0003	0.00231	0.04078
Diffuse-visible	−0.04109	−0.00366	−0.00031	0.00315	0.05535
Direct-visible	−0.03508	−0.00405	−0.00042	0.00279	0.05147
NIR	−0.1613	−0.01259	0.00263	0.01537	0.07276
Diffuse-NIR	−0.1713	−0.00778	0.00124	0.00873	0.08364
Direct-NIR	−0.1816	−0.0133	0.00294	0.01619	0.07911

objectives of the "VEGETATION" system are to provide accurate measurements of basic characteristics of vegetation canopies on an operational basis, either for scientific studies involving both regional and global scales experiments over long time periods, or for systems designed to monitor important vegetation resources, like crops, pastures, and forests.

The fitted equations are presented below (Eq. (17)).

$$\alpha_{\text{short}} = -0.0022 + 0.3512\alpha_1 + 0.1629\alpha_2 + 0.3415\alpha_3 + 0.1651\alpha_4$$

$$\alpha_{\text{visible}} = 0.0033 + 0.5717\alpha_1 + 0.4277\alpha_2$$

$$\alpha_{\text{diffuse-visible}} = 0.0029 + 0.6601\alpha_1 + 0.3391\alpha_2$$

$$\alpha_{\text{direct-visible}} = 0.0034 + 0.5310\alpha_1 + 0.4684\alpha_2$$

$$\alpha_{\text{NIR}} = -0.0038 + 0.6799\alpha_3 + 0.3157\alpha_4$$

$$\alpha_{\text{diffuse-NIR}} = -0.0040 + 0.8495\alpha_3 + 0.1350\alpha_4$$

$$\alpha_{\text{direct-NIR}} = -0.0033 + 0.6567\alpha_3 + 0.3382\alpha_4. \quad (17)$$

The results are also presented in Figs. 21 and 22, the summaries of the fitted residuals are presented in Table 9. VEGETATION has the same number of bands as MISR, but it seems to produce better predictions in most cases.

5. Summary

Narrowband albedos retrieved from high-resolution remotely sensed data need to be converted to broadband albedos that are required by various scientific applications. The previous studies in the literature largely rely on surface measurements under the limited atmospheric and surface conditions and produce quite different formulae even for the same sensor. This study, based on extensive radiative transfer simulations that incorporated many surface reflectance spectra and the atmospheric conditions, provides the conversion formulae for many different narrowband sensors. Moreover, most of the previous studies mainly calculate the total shortwave albedo of the specific sensors, but we also have produced the conversion formulae for calculating

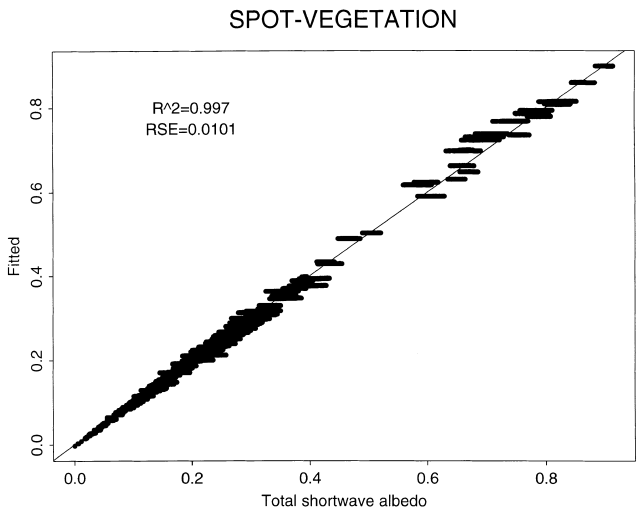

Fig. 21. Simulated total shortwave albedo and predicted by VEGETATION narrowband albedos.

direct-, diffuse-, and total-visible and near-IR albedos for multiple sensors in this study.

Although we have not been able to validate all these conversion formulae using extensive ground measurements, AVHRR and Landsat conversion formulae have been compared with existing formulae published in the literature for different surface types and good agreements were observed. Since all data sets were created using the same simulation approach, we feel confident that the conversion formulae for other sensors should be reliable.

For all the narrowband sensors evaluated in this study, the total shortwave and visible albedos can be accurately computed, and the total near-IR albedo is less accurately estimated. Diffuse visible and near-IR albedos are highly correlated with the total visible and near-IR albedos. But direct visible and near-IR albedos are more sensitive to variations in the atmospheric conditions. The fitting accuracies are lower.

If we compare different sensors, we can see that ASTER, AVHRR, MISR, POLDER, and VEGETATION have the similar ability to predict the total shortwave albedo, but ETM+/TM and MODIS produce almost as half the RSE as that produced by other sensors because of more narrowbands available in the reflective spectrum. Moreover, MODIS is also better than ETM+/TM. Although ASTER has the largest number of narrowbands in the visible and near-IR spectrum (see Table 1), most bands are in the near-IR region and apparently are not the best for distinguishing different surface reflectance spectra. GOES has been widely used for producing land surface total shortwave albedo, but our results indicate that it is a very bad predictor.

For the total visible albedo, all sensors can predict very well except AVHRR that has only one band with a larger scattering pattern, and MODIS, MISR, and ETM+ perform the best. For the total near-IR albedo, the sensors can be

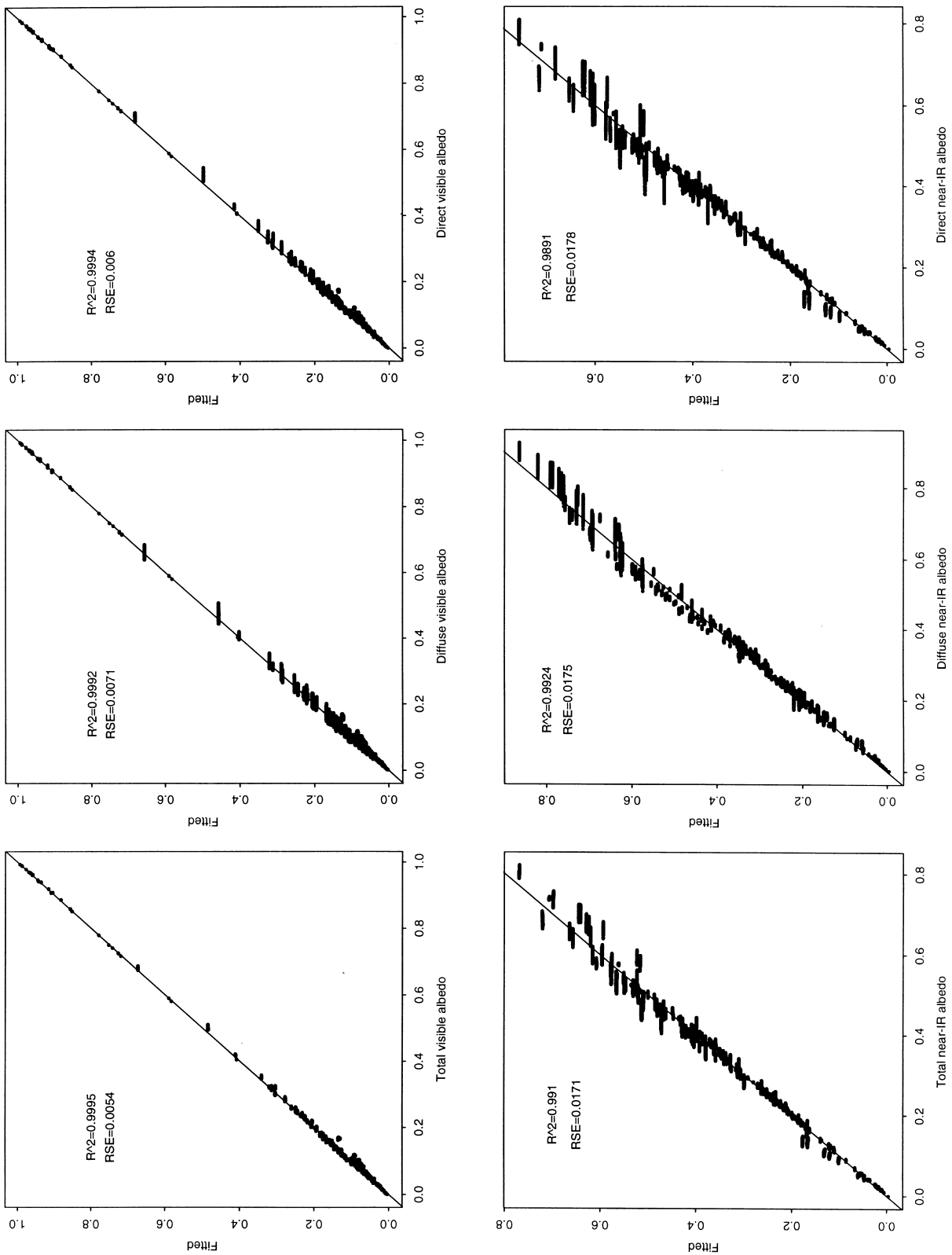

Fig. 22. Simulated broadband visible and near-IR albedos (total, direct, and diffuse) and predicted by VEGETATION narrowband albedos.

Table 9
Summary of the VEGETATION fitting residuals

Albedo	Min	1Q	Median	3Q	Max
Shortwave	−0.0654	−0.00471	−0.00016	0.00409	0.05029
Visible	−0.01242	−0.0029	−0.00118	0.00149	0.03706
Diffuse-visible	−0.02467	−0.0033	−0.00102	0.002359	0.04862
Direct-visible	−0.01798	−0.00315	−0.00121	0.00166	0.04727
NIR	−0.07742	−0.00505	0.00122	0.00441	0.08866
Diffuse-NIR	−0.07233	−0.00889	0.00183	0.00746	0.08402
Direct-NIR	−0.1186	−0.0048	0.00131	0.00432	0.09301

ordered based on their performances from the best to the worst: MODIS, ETM+/TM, VEGETATION, ASTER, POLDER, MISR, GOES, and AVHRR.

By examining all cases, it appears that MODIS is the best sensor to convert narrowband to broadband albedos. However, it does not mean the MODIS broadband albedos will be the most accurate products because the uncertainties for calculating narrowband albedos can also affect the accuracy of the final broadband albedo products. Since the conversion formulae are primarily linear, conducting sensitivity study is straightforward, and no detailed discussions will be given here.

Because the angular dependences of these surface reflectance spectra are not available, we simply assumed that these land surfaces are Lambertian (isotropic in reflectance) in our simulation. The Lambertian assumption may be far from the actual situations. However, this assumption was only for calculating the spectral distribution of downward flux. It is known that the spectral downward sky radiance and the integrated flux are not very sensitive to the anisotropy of surface reflectance (e.g., Liang & Lewis, 1996). Therefore, this assumption should not impact the derived formulae in this study.

All formulae discussed earlier are only suitable for converting land surface narrowband albedos to broadband albedos. The satellite TOA narrowband observations need to be converted into surface albedos through the atmospheric correction procedure. The Terra science teams will produce surface narrowband albedos for ASTER, MISR, and MODIS, and the POLDER team will also produce surface narrowband albedos. For AVHRR and TM/ETM+ users, an atmospheric correction procedure needs to be applied although it is not trivial. Since TOA satellite observations contain both atmospheric and surface information and broadband surface albedos are sensitive to both properties, it is possible to make the direct linkages between TOA observations and broadband shortwave albedos. We explored this in our previous study by using a neural network method (Liang et al., 1999). Because of the scope, the further exploration of this topic is beyond this paper.

Atmospheric correction produces surface spectral reflectance. If the surface is a Lambertian, spectral reflectance is equal to spectral albedo. For multiangle observations, this is also a less important issue. Otherwise, certain algorithms are needed to generate spectral albedo. For example, the MODIS science team converted spectral reflectance to spectral albedo based on observations accumulated during the period of 16 days (Lucht et al., 2000). Another method is to classify land surfaces and develop an angular model for each cover type (e.g., CERES algorithm, Wielicki et al., 1998). A detailed discussion of these models and algorithms is beyond this paper, the interested readers are referred to our recent review paper (Liang, Stroeve, et al., 2000).

In this study, we employed 256 surface reflectance spectra in the simulation, much larger than a dozen of reflectance spectra commonly used in the most previous simulation studies. Although a procedure was used in this study that enables us to incorporate as many reflectance spectra as we want and more surface reflectance spectra are actually available now from the handheld radiometers or airborne remotely sensed data, it is unnecessary to use every available reflectance curve. However, whether these 256 reflectance spectra are really representative enough still needs to be verified in the future by using extensive ground measurements under different conditions. From the comparisons with other published conversion equations, we are convinced that this database is very comprehensive and reliable. Since most conversion formulae are linear, they should be valid for any linear mixtures of these reflectance spectra. The validation results based on ground measurements will be presented in the companion paper (Liang, Shuey, et al., 2000).

Acknowledgments

The author would like to thank Dr. Mingzhen Chen for his processing AVIRIS imagery, Dr. Wolfgang Lucht for his valuable discussions, and Dr. Crystal Schaaf for her comments on the early draft of the paper. Valuable comments from three anonymous reviewers are greatly appreciated. This work is partly supported by the National Aeronautics and Space Administration under grants NAG5-6459 and NCC5462.

References

Brest, C. L., & Goward, S. (1987). Deriving surface albedo measurements from narrowband satellite data. *International Journal of Remote Sensing*, *8*, 351–367.

Cess, R. D. (1978). Biosphere-albedo feedback and climate modeling. *Journal of the Atmospheric Sciences*, *35*, 1765–1768.

Clark, R. N., Swayze, G. A., Gallagher, A. J., King, T. V. V., & Calvin, W. M. (1993). The U.S. Geological Survey digital spectral library: version 1: 0.2 to 3.0 microns. U.S. Geological Survey Open File Report 93-592, 1340 pp.

Csiszar, I., & Gutman, G. (1999). Mapping global land surface albedo from NOAA AVHRR. *Journal of Geophysical Research*, *104*, 6215–6228.

Deschamps, P. Y., Brion, F., Leroy, M., Podaire, A., Bricaud, A., Buriez, J., & Seze, G. (1994). The POLDER mission: instrument characteristics and scientific objectives. *IEEE Transactions on Geoscience and Remote Sensing*, *32*, 598–615.

Dickinson, R. E. (1983). Land surface processes and climate-surface albedos and energy balance. *Advances in Geophysics*, *25*, 305–353.

Diner, D., Beckert, J. C., Reilly, T. H., Bruegge, C. J., Conel, J. E., Kahn, R. A., Montonchik, J., Ackerman, T. P., Davies, R., Gerstl, S. A. W., Gordon, H. R., Muller, J.-P., Myneni, R. B., Sellers, P. J., Pinty, B., & Verstraete, M. M. (1998). Multi-angle Imaging SpectroRadiometer (MISR) instrument description and experiment overview. *IEEE Transactions on Geoscience and Remote Sensing*, *36*, 1072–1087.

Dorman, J. L., & Sellers, P. J. (1989). A global climatology of albedo, roughness length and stomatal resistance for atmospheric general circulation models as represented by the Simple Biosphere model SiB. *Journal of Applied Meteorology*, *28*, 833–855.

Duguay, C. R., & LeDrew, E. F. (1992). Estimating surface reflectance and albedo from Landsat-5 Thematic Mapper over rugged terrain. *Photogrammetric Engineering and Remote Sensing*, *58*, 551–558.

Gratton, D. J., Howart, P. J., & Marceau, D. J. (1993). Using Landsat-5 thematic mapper and digital elevation data to determine the net radiation field of a mountain glacier. *Remote Sensing of the Environment*, *43*, 315–331.

Green, R., Eastwood, M. L., & Williams, O. (1998). Imaging spectroscopy and the airborne visible/infrared imaging spectrometer (AVIRIS). *Remote Sensing of the Environment*, *65*, 227–248.

Gutman, G. G. (1994). Global data on land surface parameters from NOAA AVHRR for use in numerical climate models. *Journal of Climate, 7,* 699–703.

Han, W., Stamnes, K., & Lubin, D. (1999). Remote Sensing of surface and cloud properties in the arctic from AVHRR measurements. *Journal of Applied Meteorology*, *38*, 989–1012.

Jacobowitz, H., Tinghe, R. J., and the Nimbus-7 ERB Experiment Team. (1984), The earth radiation budget derived from the Nimbus-7 ERB experiment. *Journal of Geophysical Research, 89,* 4997–5010.

Kandel, R., Viollier, M., Raberanto, P., Duvel, J. P., Pakhomov, L. A., Golovko, V. A., Trishchenko, A. P., Mueller, J., Rashke, E., & Stuhlmann, R. (1998). The ScaRaB earth radiation budget dataset. *Bulletin of the American Meteorology Society*, *79*, 765–783.

Key, J. (1996). *The cloud and surface parameter retrieval (CASPR) system for polar AVHRR, version 1.0: user's guide*. Boston: Boston University.

Kiehl, J. T., Hack, J. J., Bonan, G. B., Boville, B. A., Briegleb, B. P., Williamson, D. L., & Rasch, P. J. (1996). Description of the NCAR Community Climate Model. NCAR Technical Note NCAR/TN-420+STR, National Center for Atmospheric Research, Boulder, Colorado, 152 pp.

Kimes, D. S., & Holben, B. N. (1992). Extracting spectral albedo from NOAA-0 AVHRR multiple view data using an atmospheric correction procedure and an expert system. *International Journal of Remote Sensing*, *13*, 275–289.

King, M., & Greenstone, R. (Eds.). (1999). *EOS reference handbook, a guide to NASA's Earth Science Enterprise and the Earth Observing System,* Greenbelt, Maryland, USA: NASA, NP-1999-08-134-GSFC (361 pp.).

Knap, W., Reijmer, C., & Oerlemans, J. (1999). Narrowband to broadband conversion of Landsat TM glacier albedos. *International Journal of Remote Sensing*, *20*, 2091–2110.

Koster, R., & Suarez, M. (1992). Modeling the land surface boundary in climate models as a composite of independent vegetation stands. *Journal of Geophysical Research*, *97*, 2697–2715.

Li, Z., & Leighton, H. (1992). Narrowband to broadband conversion with spatially autocorrelated reflectance measurements. *Journal of Applied Meteorology*, *31*, 421–432.

Liang, S., Fallah-Adl, H., Kalluri, S., JaJa, J., Kaufman, Y., & Townshend, J. (1997). Development of an operational atmospheric correction algorithm for TM imagery. *Journal of Geophysical Research*, *102*, 17173–17186.

Liang, S., & Lewis, P. (1996). A parametric radiative transfer model for sky radiance distribution. *Journal of Quantitative Spectroscopy & Radiative Transfer*, *55*, 181–189.

Liang, S., Shuey, C., Fang, H., Walthall, C., Daughtry, C., & Hunt, R. (2000). Narrowband to broadband conversions of land surface albedo: II. Validation. *Remote Sensing of the Environment*, submitted.

Liang, S., Strahler, A., & Walthall, C. (1999). Retrieval of land surface albedo from satellite observations: a simulation study. *Journal of Applied Meteorology*, *38*, 712–725.

Liang, S., Stroeve, J., Grant, I., Strahler, A., & Duvel, J. (2000). Angular correction to satellite data for estimating earth's radiation budget. *Remote Sensing Review*, *18*, 103–136.

Liou, K. N. (1980). *An introduction to atmospheric radiation*. New York: Academic Press.

Lucht, W., & Roujean, J.-L. (2000). Considerations in the parametric modeling of BRDF and albedo from multiangular satellite sensor observations. *Remote Sensing Review 18, 343–380.*

Lucht, W., Schaaf, C. B., & Strahler, A. (2000). An algorithm for the retrieval of albedo from space using semiempirical BRDF models. *IEEE Transactions on Geoscience and Remote Sensing*, *38*, 977–998.

Pinker, R., Kustas, W., Laszlo, I., Moran, S., & Huete, A. (1994). Satellite surface radiation budgets on basin scale in semi-arid regions. *Water Resources Research*, *30*, 1375–1386.

Pinker, R. T., Frouin, R., & Li, Z. (1995). A review of satellite methods to derive surface shortwave irradiance. *Remote Sensing of the Environment*, *51*, 108–124.

Ranson, K. J., Irons, J. R., & Daughtry, C. S. T. (1991). Surface albedo from bidirectional reflectance. *Remote Sensing of the Environment*, *35*, 201–211.

Ricchiazzi, P., Yang, S., Gautier, C., & Sowle, D. (1998). SBDART: a research and teaching software tool for plane-parallel radiative transfer in the earth's atmosphere. *Bulletin of the American Meteorological Society*, *79*, 2101–2114.

Russell, M., Nunez, M., Chladil, M., Valiente, J., & Lopez-Baeza, E. (1997). Conversion of nadir, narrowband reflectance in red and near-infrared channels to hemispherical surface albedo. *Remote Sensing of the Environment*, *61*, 16–23.

Sato, N., Sellers, P. J., Randall, D. A., Schneider, E. K., Shukla, J., Kinter, J. L. III, Hou, Y. T., & Albertazzi, E. (1989). Effects of implementing the simple biosphere model (SiB) in the general circulation model. *Journal of the Atmospheric Sciences*, *46*, 2757–2782.

Saunders, R. W. (1990). The determination of broad band surface albedo from AVHRR visible and near-infrared radiances. *International Journal of Remote Sensing*, *11*, 49–67.

Sellers, P., Hall, F., Kelly, R., Black, A., Baldocchi, D., Berry, J., Ryan, M., Ranson, J., Crill, P., Lettenmaier, D., Margolis, H., Cihlar, J., Newcomer, J., Fitzjarrald, D., Jarvis, P., Gower, S., Halliwell, D., Williams, D., Goodison, B., Wickland, D., & Guertin, F. (1997). BOREAS in 1997: experiment overview, scientific results, and future directions. *Journal of Geophysical Research*, *102*, 28731–28769.

Sellers, P., Randall, D. A., Collatz, G. J., Berry, J. A., Field, C. B., Dazlich, D. A., Zhang, C., Collelo, G. D., & Bounoua, L. (1996). A revised land surface parameterization (SiB2) for atmospheric GCMs: Part I. Model formulation. *Journal of Climate*, *9*, 676–705.

Shukla, J. & Dirmeyer, P. A. (1994). Albedo as a Modulator of Climate Response to Tropical Deforestation. *Journal of Geophysical Research, 99,* 20863–20878.

Smith, G. L., Green, R. N., Raschke, E., Avis, L. M. Suttles, J. T., Wielicki, B. A. & Davies, R. (1986). Inversion methods for satellite studies of the earth's radiation budget: development of algorithms for the ERBE mission. *Reviews in Geophysics, 24,* 407–421.

Song, J., & Gao, W. (1999). An improved method to derive surface albedo from narrowband AVHRR satellite data: narrowband to broadband conversion. *Journal of Applied Meteorology*, *38*, 239–249.

Stroeve, J., Nolin, A., & Steffen, K. (1997). Comparison of AVHRR-derived and in-situ surface albedo over the Greenland ice sheet. *Remote Sensing of the Environment*, *62*, 262–276.

Strugnell, N., & Lucht, W. (2000). Continental-scale albedo inferred from

AVHRR data, land cover class and field observations of typical BRDFs. *Journal of Climate*, (in press).

Townshend, J. G. R. (1994). Global data sets for land applications from the Advanced Very High Resolution Radiometer: an introduction. *International Journal of Remote Sensing*, *15*, 3319–3332.

Valiente, J., Nunez, M., Lopez-Baeza, E., & Moreno, J. (1995). Narrow-band to broad-band conversion for Meteosat-visible channel and broad-band albedo using both AVHRR-1 and -2 channels. *International Journal of Remote Sensing*, *16*, 1147–1166.

Wielicki, B. A., Barkstrom, B. R., Baum, B. A., Charlock, T. P., Green, R. P., Kratz, D. P., Lee, R. B. III, Minnis, P., Smith, G. L., Wong, T., Young, D. F., Cess, R. D., Coakley, J. A. Jr., Crommelynck, D. A., Donner, L., Kandel, R., King, M. D., Miller, A. J., Ramanathan, V., Randall, D. A., Stowe, L. L., & Welch, R. M. (1998). Clouds and the Earth's Radiant Energy System (CERES): algorithm overview. *IEEE Transactions on Geoscience and Remote Sensing*, *36*, 1127–1141.

Wydick, J. E., Davis, P. A. & Gruber, A. (1987). Estimation of broadband planetary albedo from operational narrowband satellite measurements. NOAA Technical Report NESDIS 27, April 1987.

Xue, Y., Sellers, P., Kinter, J. III, & Shukla, J. (1991). A simplified biosphere model for global climate studies. *Journal of Climate*, *4*, 345–364.

Yamaguchi, Y., Kahle, A. B., Pniel, M. Overview of Advanced Spaceborne Thermal Emission and Reflection Radiometer (ASTER). *IEEE Transactions on Geosciences and Remote Sensing, 36,* 1062–1071.